ANNUAL REVIEWS

Annual Review of Earth and Planetary Sciences

Fracture Energy and Breakdown Work During Earthquakes

Massimo Cocco,[1] Stefano Aretusini,[1] Chiara Cornelio,[1] Stefan B. Nielsen,[2] Elena Spagnuolo,[1] Elisa Tinti,[1,3] and Giulio Di Toro[1,4]

[1]Sezione Roma 1, Istituto Nazionale di Geofisica e Vulcanologia, Rome, Italy

[2]Department of Earth Sciences, University of Durham, Durham, United Kingdom

[3]Dipartimento di Scienze della Terra, Università di Roma Sapienza, Rome, Italy

[4]Dipartimento di Geoscienze, Università degli Studi di Padova, Padua, Italy; email: giulio.ditoro@unipd.it

Annu. Rev. Earth Planet. Sci. 2023. 51:217–52

First published as a Review in Advance on January 6, 2023

The *Annual Review of Earth and Planetary Sciences* is online at earth.annualreviews.org

https://doi.org/10.1146/annurev-earth-071822-100304

Keywords

fracture energy, breakdown work, dynamic weakening, rupture dynamics, earthquake energy budget, fault zone structure

Abstract

Large seismogenic faults consist of approximately meter-thick fault cores surrounded by hundreds-of-meters-thick damage zones. Earthquakes are generated by rupture propagation and slip within fault cores and dissipate the stored elastic strain energy in fracture and frictional processes in the fault zone and in radiated seismic waves. Understanding this energy partitioning is fundamental in earthquake mechanics to explain fault dynamic weakening and causative rupture processes operating over different spatial and temporal scales. The energy dissipated in the earthquake rupture propagation along a fault is called fracture energy or breakdown work. Here we review fracture energy estimates from seismological, modeling, geological, and experimental studies and show that fracture energy scales with fault slip. We conclude that although material-dependent constant fracture energies are important at the microscale for fracturing grains of the fault zone, they are negligible with respect to the macroscale processes governing rupture propagation on natural faults.

- Earthquake ruptures propagate on geological faults and dissipate energy in fracture and frictional processes from micro- (less than a millimeter) to macroscale (centimeters to kilometers).

- The energy dissipated in earthquake rupture propagation is called fracture energy (G) or breakdown work (W_b) and scales with coseismic slip.
- For earthquake ruptures in natural faults, the estimates of G and W_b are consistent with a macroscale description of causative processes.
- The energy budget of an earthquake remains controversial, and contributions from different disciplines are required to unravel this issue.

1. INTRODUCTION

Earthquakes are caused by a shear rupture instability along a fault that undergoes a sudden displacement of the rocks on either side of the fault called slip. A fault is a zone of weakness with fractures between two hosting blocks (wall rocks), called the fault zone, which can move rapidly (~1 m/s), generating an earthquake, or slowly (up to 1 cm/year) in the form of nearly stable sliding and creep (Scholz 2019). Faults may range in length from millimeters to thousands of kilometers. The sudden motion of the fault is associated with the propagation of a rupture front generating the seismic waves radiated away from the source in Earth's crust (Aki 1980, Kostrov & Das 1988).

Tectonic stress accumulates within a fault zone because of strain localization in Earth's brittle crust (Cowie et al. 2006). This yields faults producing repeated displacements and sometimes earthquakes over geologic times. The repeated occurrence of earthquakes defines the seismic cycle of a fault. The tectonic stress is applied at a slow and possibly steady rate to a fault in the brittle crust (Reid 1910) during the interseismic period (see **Figure 1**). Prior to an earthquake, slip increases quasi-statically in single or distinct episodes during the so-called nucleation phase in a limited portion of the fault zone volume (preseismic), from which the dynamic rupture propagates away over a much larger area of the fault. The latter defines the coseismic phase in which the

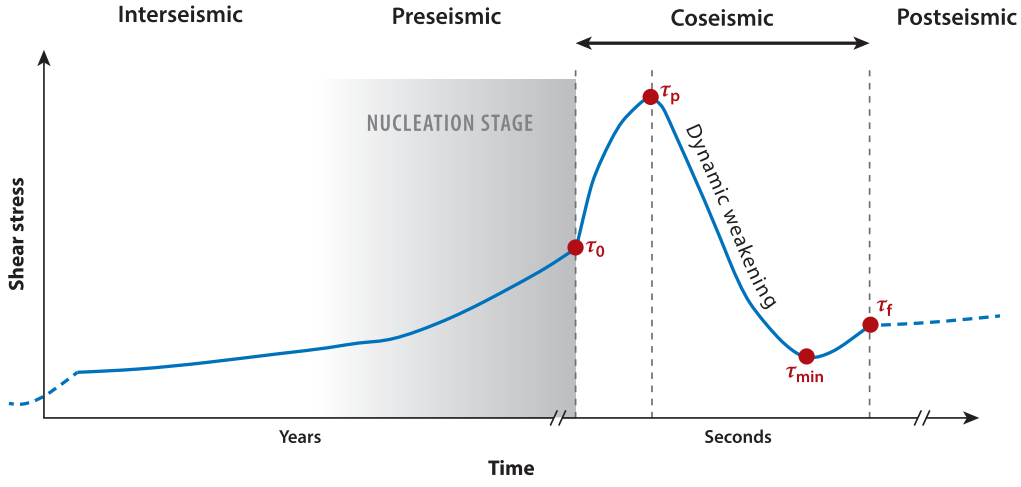

Figure 1

Shear stress evolution with time in a single point of the fault before, during, and after the passage of an earthquake rupture. According to this conceptual model, shear stress is accumulated in the fault zone volume during the interseismic phase and reaches τ_0. The coseismic phase starts when the fault slips and rupture is propagating dynamically. This is associated with the shear stress evolution from its initial value τ_0 up to its final value τ_f. The shear stress decrease from its peak value τ_p to the minimum value τ_{min} defines the dynamic weakening or breakdown stage. Nucleation of an earthquake rupture occurs in the preseismic phase in a limited volume of the fault zone preceding the dynamic rupture propagation.

elastic strain energy stored in the fault zone is released near the propagating rupture front. The coseismic phase ends with the healing of slip and rupture arrest on the whole fault. The coseismic phase is followed by the postseismic phase in which the released stress is redistributed around the source volume and the interseismic phase when stress buildup starts again until the next earthquake occurs. In this review, we cover the energy budget during a single earthquake and focus on the coseismic phase, characterized by the shear stress evolution from an initial shear stress τ_0 to a final shear stress τ_f. This evolution with time and slip includes the dynamic weakening or breakdown stage defined by the decrease of the shear stress from its peak value τ_p to a minimum or residual stress level τ_{min} (**Figure 1**).

Geological observations evidence the occurrence of extreme (often less than 1-cm thick) coseismic slip localization from the lower to the upper crust (Austrheim & Boundy 1994, Chester & Chester 1998, Demurtas et al. 2016, Di Toro et al. 2005b, Fondriest et al. 2013, Rowe et al. 2005, Sibson 2003, Siman-Tov et al. 2013, Swanson 1988, Ueda et al. 2008, Wibberley & Shimamoto 2003). These so-called principal slip zones (PSZs) of finite thickness, limited by continuous surfaces called fault surfaces, sustain coseismic displacement and dynamic reduction of shear resistance and are embedded in a fault core (FC), where most of the displacement is accommodated, surrounded by a plastic zone with fractures called a damage zone (DZ) (Caine et al. 1996; Chester & Logan 1986; Chester et al. 1993, 2004; Choi et al. 2016; Dor et al. 2006; Faulkner et al. 2010, 2011; Fondriest et al. 2015; Mitchell & Faulkner 2009; Ostermeijer et al. 2020; Savage & Brodsky 2011; Vermilye & Scholz 1998; Wibberley et al. 2008) (**Figure 2**). The FC can contain single or multiple PSZs made of gouges or foliated gouges (noncohesive fault rocks) or cataclasite, breccia, or pseudotachylytes (cohesive fault rocks), while the DZ has a higher fracture density than the

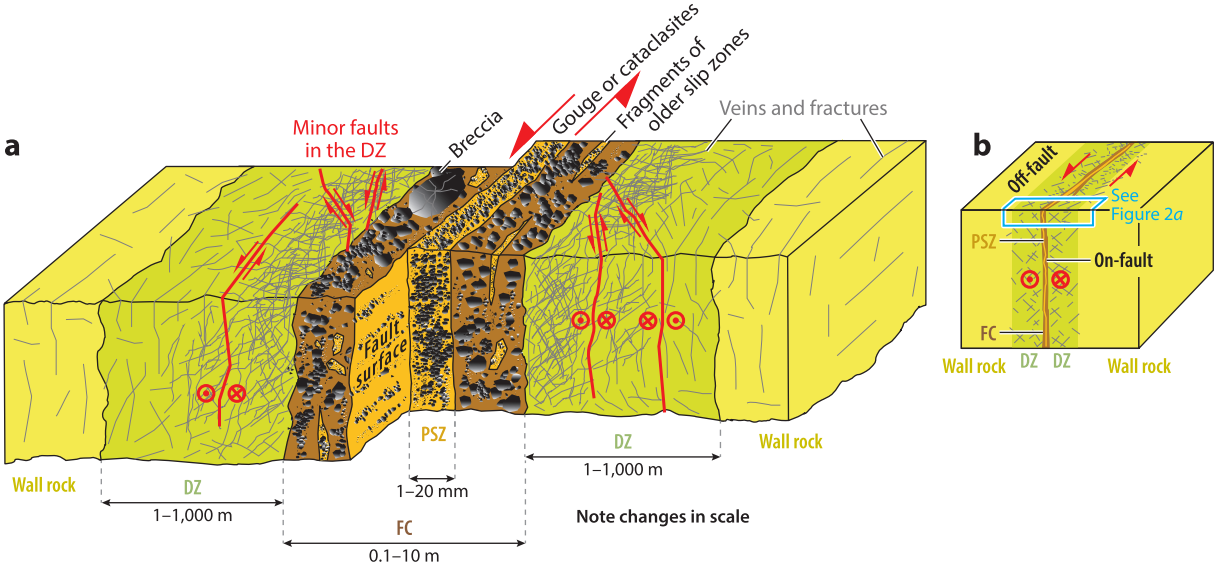

Figure 2

Model of a seismogenic fault zone structure. (*a*) Fault zone composed of a damage zone (DZ) containing a fault core (FC) where strain is localized within a principal slip zone (PSZ) and available energy is released by coseismic slip during earthquakes. According to this fault zone model, the PSZ is made of gouges (noncohesive rock powders) or cataclasites (lithified gouges), and the FC is made of cataclasites/gouges, fault breccia, and fragments of older PSZs. The DZ is cut by minor faults (*red in color*) and veins and fractures (*gray in color*). The scale changes from the PSZ (thickness of 1–20 mm) to the DZ (thickness of 1–1,000 m). (*b*) Conceptual fault zone structure composed of a DZ containing an FC of finite thickness sustaining coseismic slip also along PSZs (*red in color*).

surrounding wall rocks. There is a high level of subjectivity in the definition of the boundaries of FC and DZ because they depend on lithology, fracture distribution, rheology, and strain rate during deformation (Shipton et al. 2006, Choi et al. 2016). The thickness of the FC can be on the order of meters while the one of DZs can be up to several hundreds of meters (Fondriest et al. 2020). For the purposes of this review, we follow a simplified model in which the fault zone structure is composed of an FC of finite thickness sustaining shear displacement (coseismic slip) along single or multiple PSZs embedded in a fractured DZ (**Figure 2*b***).

Recent seismological and geodetic observations have corroborated the evidence that active faults are characterized by a wide range of slip behaviors that include aseismic creep events, slow-slip and low-frequency events, afterslip, and earthquakes (Harris 2017, Ikari et al. 2015, Peng & Gomberg 2010). Although the physical mechanisms responsible for this multi-mode slip behavior are poorly understood, the response of a fault zone to tectonic loading and strain localization depends on its structure (geometry and spatial dimensions) and composition (lithology and rheology) (Scholz 2019). Furthermore, the dynamic fault instability caused by the sudden release of stored elastic strain energy and associated with the fault weakening and slip acceleration is described by both fracture and frictional processes (Ohnaka 2013), likely occurring at different spatial and temporal scales. Microscale processes affect rupture and slip episodes at the scale of the rocks composing the fault gouge (0.1–10 mm), while macroscale processes control the fault zone response and the dynamic reduction of shear resistance at the scale of fault patches (1–1,000 m) (for reviews, see Delle Piane et al. 2017, Niemeijer et al. 2012, Tullis 2015). The comprehensive discussion of the scale dependence of earthquake ruptures is beyond the scope of this article. Instead, here we address the issue of the energy dissipated on the fault during the coseismic rupture propagation with the ambition to reconcile the geological observations of fault zones with seismological and geodetic observations of earthquake ruptures as well as with laboratory experiments.

During the interseismic period, energy builds up in the volume surrounding the fault due to tectonic loading (**Figure 1**). Earthquake rupture is driven by a sudden transfer of strain energy (elastic and gravitational, ΔW) from the wall rocks into radiated energy (elastic waves, E_R) and dissipated energy in the fault zone (crystal plastic, fracture, and friction, E_{FZ}) (symbols are listed in **Table 1**):

$$\Delta W = E_R + E_{FZ} \quad (\text{in Joule}). \qquad 1.$$

These energies are integral quantities representative of the whole fault. The energy dissipated at a single point of the fault is represented by the energy density (or work per unit area, J/m^2). However, radiated energy can be estimated only for the whole fault and cannot be mapped or associated with a specific point on the fault (Rivera & Kanamori 2005, Udias et al. 2014). Here we are interested in discussing the energy density dissipated within the fault zone (W_{FZ}), which is assumed to be partitioned in energy or work density dissipated in the propagation of the rupture front (W_G), energy density dissipated on-fault through fracture and frictional processes acting in the FC (W_{on}), and energy density lost off-fault in the DZ (W_{off}) (Andrews 2005, Rice et al. 2005):

$$W_{FZ} = W_G + W_{off} + W_{on} \quad \left(\text{in Joule}/\text{m}^2\right). \qquad 2.$$

This formulation of the energy dissipation depends on the structure adopted for the fault zone. Here we rely on the fault structure depicted in **Figure 2*b***, where we consider on-fault all processes occurring within the FC and off-fault those occurring in the DZ. Quantifying the partitioning and the relative weight of these energy dissipation mechanisms is a challenge currently addressed by model-dependent interpretations (Okubo et al. 2019). In this review we discuss the different interpretative frameworks proposed to address the issue of the mechanical work dissipated on faults during earthquake ruptures. The energy density W_G dissipated in earthquake rupture propagation at relatively high speeds (~km/s) is usually called fracture energy (G) (Ohnaka 2013, Scholz

Table 1 List of symbols and acronyms

Symbols and acronyms used in the main text	
α	Slip exponent
γ	Specific surface energy (J/m^2)
δ	Coseismic slip (m)
δ_i	Slip in the i-th cell of the discretized fault plane (m)
$\dot{\delta}$	Coseismic slip rate (m/s)
δ_{tot}	Final slip in a given point of the fault (m)
$<\delta_{tot}>$	Final average slip at ξ (m)
Γ	Energy density measured in stick-slip experiments (J/m^2)
μ	Rigidity (Pa)
μ_d	Dynamic friction coefficient
μ_s	Static friction coefficient
Σ	Final fault area (m^2)
$\Delta\sigma$	Brune stress drop (Pa)
σ_a	Apparent stress (Pa)
σ_n	Normal stress (Pa)
σ_n^{eff}	Effective normal stress (Pa)
τ	Shear stress (Pa)
$\Delta\tau_b$	Breakdown stress drop (Pa)
$\Delta\tau_d$	Dynamic stress drop (Pa)
τ_f	Final stress, shear stress at the end of the coseismic phase (Pa)
τ_{min}	Minimum shear stress level (Pa)
τ_p	Peak shear stress (Pa)
$\Delta\tau_s$	Static stress drop (Pa)
τ_r	Residual shear stress (Pa)
τ_y	Yield stress (Pa)
τ_0	Initial shear stress (Pa)
D_a	Slip at τ_p (m)
D_c	Slip-weakening distance (m)
D_w, D_{th}	Thermal weakening distance (m)
E_{FH}	Frictional energy (heat) (J)
E_{FZ}	Energy dissipated in the fault zone (J)
E_G	Total fracture energy (J)
E_R	Radiated energy (J)
$\Im_f$	Frictional work density (J/m^2)
G	Fracture energy (J/m^2)
G'	Seismological fracture energy (J/m^2)
G_{IIC}	Shear fracture energy from laboratory experiments (J/m^2)
H	Frictional heat per unit fault area (**Figure 5*a***) (J/m^2)
L	Rupture (crack) length (m)
M_0	Seismic moment (Nm)
r	Source radius (m)
R	Breakdown zone
SZ	Slipping zone length (m)

(*Continued*)

Table 1 (*Continued*)

Symbols and acronyms used in the main text	
t	Time (s)
T	Temperature (°C)
t_b, T_b	Breakdown time (s)
t_h	Slip healing time (s)
t_r	Rupture time (s)
U_f	Total macroscopic frictional work (J)
V_r	Rupture velocity (m/s)
ΔW	Total strain energy variation (J)
W_b	Breakdown work (J/m^2)
W_{FZ}	Energy density dissipated in the fault zone (J/m^2)
W_G	Energy density dissipated in rupture propagation (J/m^2)
W_{off}	Energy density dissipated off-fault (J/m^2)
W_{on}	Energy density dissipated on-fault (J/m^2)
PSZ	Principal slipping zone
FC	Fault core
DZ	Damage zone
Symbols used in the Supplemental Text	
γ_{eff}	Effective surface energy (J/m^2)
G_o	Energy release rate (J/m^2)
K	Stress intensity factor (Pa m$^{1/2}$)
E	Young's modulus (Pa)
$\Delta\tau$	Stress drop (Pa)
h	Thickness of the principal slipping zone PSZ (m)
$L(t)$	Crack length as a function of time (m)

Supplemental Material >

2019, and references therein). Here, after introducing the theoretical framework to define W_{FZ} and G, we discuss how they are related to the modeling of shear stress evolution as a function of time, slip, and slip rate. Then, we define frictional and breakdown work (Section 2) and show how part of the frictional dissipation computes into fracture energy (Section 3). In Sections 4–5, we show how field evidence and rupture modeling are used to quantify energy sinks (fracture surface energy) that occur within the FC and in a wider off-fault DZ, and we discuss how the latter sinks can contribute to the fracture energy computation. Subsequently, we discuss how G is estimated from seismological observations, on one hand (Section 6), and how it is measured in laboratory experiments, on the other hand (Section 7). Finally, we discuss how the different estimates compare to each other and how they are intrinsically related to the scale of the ruptures (Section 8).

2. FRICTIONAL AND BREAKDOWN WORK

Earthquake dynamics is commonly described by constitutive equations governing the coseismic rupture and the associated fault weakening process (Bizzarri 2011, Ohnaka 2013, Rice & Cocco 2007). Dynamic fault weakening is described by shear stress evolution, and the governing constitutive equation is represented by expressing shear stress (τ) as a function of slip (δ), slip rate ($\dot{\delta}$), temperature (T), effective normal stress, and other constitutive parameters defining the geometrical, rheological, and poroelastic properties of the fault zone (e.g., Nielsen et al. 2008, 2021; Rice 2006). Often these physical quantities are defined within the slip zone (SZ) or on the fault surface where deformation is assumed to be localized. The adoption of a fault constitutive law is

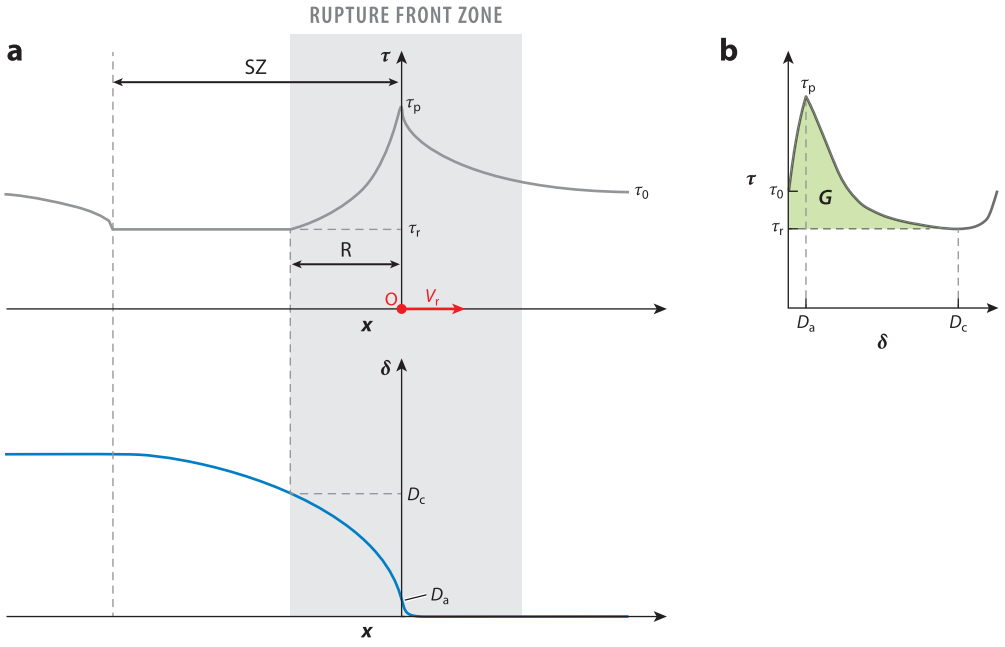

Figure 3

Spatial evolution of shear stress and slip along a propagating rupture. (*a*) The rupture front is located at O (*red circle*). The arrow shows the propagation direction of the tip, and V_r is the propagation speed. R identifies the breakdown zone, defined as the set of points behind a propagating rupture front where shear stress is decreasing from the peak value (τ_p) to the residual value (τ_r). SZ identifies the fault points that are slipping at a given time (i.e., the slipping zone). (*b*) Shear stress as a function of slip for a simplified 1D propagating rupture. Panel adapted from Ohnaka (2013). The rupture front zone (*shaded area*), which includes the breakdown zone R, is the region where shear stress evolves from the initial stress τ_0 to τ_r (Chen et al. 2021). D_c is the slip-weakening distance, and D_a is the slip at the peak stress. G is the fracture energy.

necessary to numerically solve the elastodynamic equation and model the spontaneous propagation of the earthquake rupture (Dunham et al. 2011a,b; Gallovič et al. 2019; Murphy et al. 2018; Tinti et al. 2021; Ulrich et al. 2019, among many others). The constitutive law prescribes shear stress around the rupture front and allows the dissipation of a finite energy density at the crack tip, commonly identified with the fracture energy. Two commonly adopted classes of constitutive laws are the slip-dependent (Andrews 1976a,b; Ohnaka 2013; Ohnaka & Yamashita 1989; and references therein) and rate- and state-dependent (Dieterich 1979, Marone 1998, Ruina 1983, Tullis 2015, and references therein) laws. In both formulations, dynamic weakening (or breakdown) is represented by the shear stress drop associated with slip increase resulting in the so-called slip-weakening behavior (Barenblatt 1959, Cocco & Bizzarri 2002, Ida 1972, Palmer & Rice 1973). **Figure 3** shows the stress and slip evolution for a propagating 1D crack: During its propagation, the crack tip is at point O (red circle) along the fault, and shear stress is at its peak value (τ_p), while ahead of the tip and outside the rupture front zone the shear stress is at its initial value (τ_0). The slip (D_a) at the tip (and ahead of the tip) is defined and valued by the adopted slip-dependent constitutive law (Ohnaka 2013). Behind the tip, the breakdown zone (R) identifies the set of points that are undergoing dynamic weakening (i.e., shear stress drops from the peak to the residual level). Behind the breakdown zone, the points are still slipping at the residual stress level τ_r inside the slipping zone (SZ, which includes R). Instead, **Figure 3*b*** depicts the shear stress as a function of slip, usually called the slip-weakening curve. D_c is the slip-weakening distance, defined

as the slip at the end of the dynamic weakening (breakdown) stage, when shear stress reaches its residual frictional level. The D_c value and the stress level behind the slipping zone also depend on the adopted constitutive law (Beeler 2007). The model illustrated in **Figure 3** represents a classic breakdown model through which the stress singularity at the crack tip, foreseen by linear elastic fracture mechanics (LEFM), is removed. The region defined by the stress evolution from the initial stress to the residual value is the rupture front zone (shaded area in **Figure 3**), which includes the breakdown zone R (Chen et al. 2021).

To obtain a mathematical formulation of W_{FZ} (Equation 2), we first define the total frictional work (U_f) as the irreversible part of the total strain energy change that does not go into radiated energy (Cocco et al. 2006, Kostrov & Das 1988). Although we use the term frictional work proposed by Cocco et al. (2006), the macroscopic frictional work represents the energy dissipated in the FC, for a simplified fault zone model shown in **Figure 2*b***. Therefore, the macroscopic U_f does not account only for frictional processes. Following Cocco et al. (2006):

$$U_f = \iint_{\Sigma} \Im_f dS = \iint_{\Sigma} dS \int_{t_r}^{t_h} \tau_i \dot{\delta}_i dt \quad (\text{in Joule}), \qquad 3.$$

where $\Im_f$, the frictional work density, is integrated over the whole fault surface Σ (assumed as planar and representing the final rupture area) to obtain U_f; $t_r(\vec{\xi})$ is the rupture time at a point $\vec{\xi}$ on the fault (which is the time in which slip velocity becomes nonzero); and $t_h(\vec{\xi})$ is local healing time of slip (which is the time in which slip velocity returns to zero). The difference $[t_h(\vec{\xi}) - t_r(\vec{\xi})]$ is the rise time or slip duration at a given fault position. The product between shear stress and slip velocity $[\tau_i \dot{\delta}_i]$ is the rate of frictional work density (also named power density, W/m^2) (Di Toro et al. 2011).

The $\Im_f$ is (Cocco et al. 2006, and references therein)

$$\Im_f = \int_{t_r}^{t_h} \tau_i \dot{\delta}_i dt = \int_0^{\delta_{tot}} \tau_i d\delta \quad \left(\text{in Joule/m}^2\right), \qquad 4.$$

where δ_{tot} is final seismic slip in a given fault patch. The integral on the right side of Equation 4 shows that $\Im_f$ is given by the area below the shear stress evolution with slip in each point of the fault (**Figure 4*a***). Clearly, $\Im_f$ varies with the location on the fault because the final slip is a function of the fault patch position, stress drop, etc. The $\Im_f$ is expressed through macroscopic physical quantities (shear stress, slip, and slip rate) characterizing dynamic fault weakening at the macroscale in which earthquakes occur by overcoming shear resistance and fault friction (Brodsky et al. 2020). According to this macroscopic phenomenological description, $\Im_f$ corresponds to W_{FZ}, or the energy density dissipated within the fault zone (Equation 2) and, therefore, it includes the energy densities W_G, W_{on}, and W_{off} (see **Supplemental Text Section 1**).

Because the absolute values of stress on a fault are unknown, the frictional work density cannot be measured. Therefore, Tinti et al. (2005b) defined the breakdown work W_b as the excess of work over the traction level having minimum magnitude achieved during slip $\vec{\tau}_{min}$:

$$W_b = \int_0^{t_b} \left(\vec{\tau}(t) - \vec{\tau}_{min}\right) \cdot \dot{\vec{\delta}}(t)\, dt = \int_0^{D_c} \left(\vec{\tau}(\delta) - \vec{\tau}_{min}\right) d\delta \quad \left(\text{in Joule/m}^2\right), \qquad 5.$$

where $\dot{\vec{\delta}}(t)$ and $\vec{\tau}(t)$ are the slip velocity and shear traction vectors, respectively, assumed to be collinear (at the last time step, if rake angle changes with time); t_b is the time at which the minimum traction $\vec{\tau}_{min}$ is reached at the target point (which is an estimate of the breakdown time $t_b \approx T_b$).

Supplemental Material >

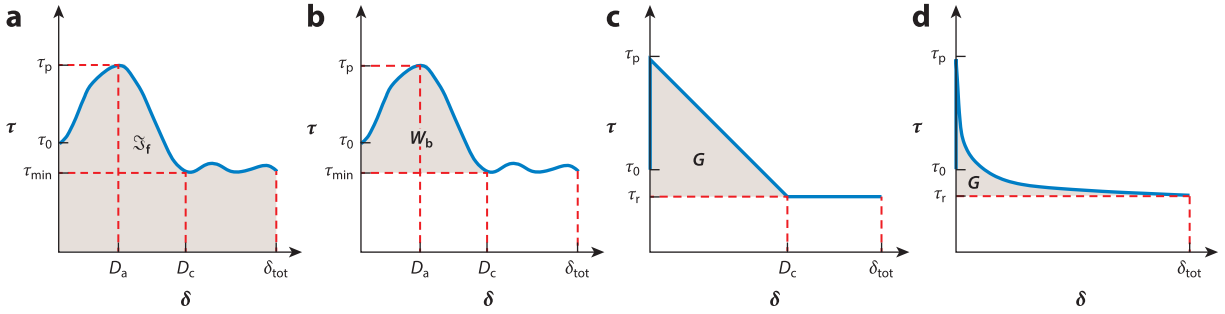

Figure 4

Examples of frictional work density ($\Im_f$), breakdown work (W_b), and fracture energy (G) at a point on the fault surface from the shear stress evolution as a function of slip δ. (*a*) $\Im_f$ measured through Equation 4. (*b*) W_b measured through Equation 5. (*c*) Ida's (1972) slip-weakening model and definition of G (Equation 7). (*d*) G inferred from a shear stress evolution with slip given by a power law (Abercrombie & Rice 2005); in this case, D_c corresponds to δ_{tot}. D_a is the slip distance at the peak stress reached during the initial stress-hardening stage.

As part of the definition of W_b, Tinti et al. (2005b) specified a way to assume the unknown initial traction vector necessary to calculate $\vec{\tau}(t)$ from the traction-change vectors derived from the kinematic slip models (**Supplemental Text Section 2**). Formulation on the right side of Equation 5 holds if the rake angle does not change with time. W_b is the portion of the frictional work associated with the breakdown stage, and it also includes the increase of stress from the initial (τ_0) to the peak (τ_p) value (**Figure 4*b***). Differently from the fracture energy inferred for Ida's (1972) slip-weakening model (**Figure 4*c***), breakdown work includes the energy dissipated during any initial slip-hardening phase consistent with the definition by Ohnaka (1996). Because the shear stress evolution during the breakdown stage determines the slip acceleration and the slip velocity time history, W_b, like G (Ida 1972), is a measure of the energy density spent to allow the rupture to advance at a determined rupture velocity (Cocco et al. 2006, Tinti et al. 2005b) (**Supplemental Text Section 2**). We discuss the relation between W_b and G in the following sections.

Supplemental Material >

3. FRACTURE ENERGY

The mechanisms explaining coseismic rupture propagation have been described as (*a*) brittle fractures or (*b*) stick-slip episodes due to frictional instabilities. Scholz (2019) emphasizes that, while approaches *a* and *b* are mathematically equivalent in describing the drop of shear stress on the fault, they substantially differ in the description of the rupture process. Here we discuss fracture energy and breakdown work definitions in relation to the earthquake rupture process, which involves both brittle fractures and frictional instabilities. In classic fracture mechanics, it is assumed that the fracture energy per unit area is a material property controlling the fracture onset and propagation (Griffith 1921, Irwin 1956), while in frictional models fracture energy depends on the adopted constitutive law and rupture propagates when the shear stress on the fault reaches static friction ($\mu_s = \tau_p/\sigma_n$) and the conditions for dynamic instability are achieved (Scholz 2019). Moreover, in fracture models stress at the crack tip is arbitrarily high or infinite, while in the frictional models shear stress at the crack tip is finite and energy dissipated at the crack tip depends on the constitutive law adopted to remove singularities.

The energy sustaining the propagation of the rupture front has been associated with the concept of crack driving force and the energy release rate for shear ruptures (see Ohnaka 2013, and references therein). As recalled in **Supplemental Text Section 1**, energy release rate scales with fracture length and the square of stress drop. In the framework of LEFM, the energy release rate

flows at the crack tip into a microscopic process zone where energy is dissipated; in the dynamic regime, energy flow at the rupture tip is modulated by a complex function of rupture velocity (Freund 1979). In this framework, fracture energy includes both the surface energy per unit area of the newly created crack and the energy required for nonelastic deformation at the tip of the extending crack (edge-localized dissipation) (Barras et al. 2020, Brener & Bouchbinder 2021). In frictional ruptures, the resistance to rupture growth can also be defined as the energy per unit area required for a rupture front to grow, further corresponding to the energy dissipated in frictional sliding on the rupture surfaces (the breakdown zone R in **Figure 3*a***). Although these two descriptions might be applied at different spatial scales (fractures at the microscale and friction at the macroscale), they yield to a similar definition of fracture energy. The necessity to remove the stress singularity at the crack tip, intrinsic in classic fracture mechanics (Irwin 1956, 1957), led to the formulation of the cohesive force models (Barenblatt 1959) for tensile cracks, further applied to shear ruptures by Ida (1972) and Palmer & Rice (1973). This yielded the formulation of the slip-weakening law, in which the spatial distribution of shear stress and slip in the breakdown zone behind the tip of a propagating rupture is expressed by a slip-dependent constitutive law (Ohnaka & Yamashita 1989). This results in the following, broadly used definition of fracture energy (Ohnaka 2013, Ohnaka & Yamashita 1989, Palmer & Rice 1973, Rice 1968):

$$G = \int_0^{D_c} [\tau(\delta) - \tau_r]\, d\delta \quad \left(\text{in Joule/m}^2\right). \tag{6.}$$

In deriving Equation 6, a constant residual stress (τ_r) independent of slip is assumed. Furthermore, in Ida's (1972) model, the increase from the initial stress to the τ_p occurs with no slip and the dynamic breakdown is described by a linear decrease of shear stress from τ_p to τ_r over a slip distance D_c. As a consequence, the fracture energy in Equation 6 is

$$G = \frac{1}{2}\left(\tau_p - \tau_r\right) D_c = \frac{1}{2}\Delta\tau_b D_c \quad \left(\text{in Joule/m}^2\right), \tag{7.}$$

where $\Delta\tau_b = (\tau_p - \tau_r)$ is the breakdown stress drop. Ohnaka (2013), based on laboratory evidence, emphasizes that the shear stress decrease with slip during the dynamic breakdown is nonlinear. Abercrombie & Rice (2005) generalized Equation 6 to compute the fracture energy per unit area G as a function of increasing slip δ in the earthquake and a slip-dependent law $\tau(\delta)$ as

$$G = \int_0^{\delta_*} \left[\tau(\delta') - \tau_r(\delta_*)\right] d\delta', \tag{8.}$$

where δ_* is the slip value at which τ_r is measured ($\delta_* = \delta_{tot}$ in **Figure 4*d***). This formulation allows the estimate of fracture energy for slip-dependent laws (e.g., power laws) for which the residual stress is a function of slip and weakening continues at a decreasing rate (**Figure 4*d***) (Rice & Cocco 2007). Equation 8 coincides with Equation 6 and LEFM (or singular crack mechanics) if τ_r is constant, meaning that $\delta_* = D_c$.

Equation 6 is a general definition of G for shear ruptures interpreted as the work required to evolve the shear stress on the principal slipping zone from the peak stress to its residual value (Palmer & Rice 1973). Equation 6 is coherent with LEFM because the inelastic work per increment of crack length is the energy release rate in the process zone. Application of Equation 6 to earthquake ruptures has, however, some limitations (Fialko 2015): (*a*) it assumes that all inelastic deformation occurs on the FC, and (*b*) it depends on the achievement of a constant τ_r. Equation 8 is more general than Equation 6 because it does not require a constant τ_r, but it still assumes that coseismic slip represents the displacement field associated with the rupture extension. We emphasize that, for a general shear stress evolution with slip $\tau(\delta)$ that can include some work dissipated

before the beginning of the dynamic weakening ($D_a \neq 0$) and collinearity with slip velocity, Equation 8 for G is equivalent to Equation 5 for W_b. In this case, breakdown work corresponds to fracture energy.

The application of Equations 6 and 8 relies on the assumption that shear stress has an explicit (as in the slip-weakening constitutive law) or implicit [as in the rate- and state-dependent constitutive laws (see Bizzarri 2010, and references therein)] dependence on coseismic slip. These definitions of fracture energy are associated with a finite breakdown stress drop and depend on the position along the fault plane because final slip, D_c, and other parameters depend on position.

In the next sections we discuss the scaling of G with slip or earthquake size, which contrasts with LEFM that considers G a material property. For this we discuss G and W_b estimates on both natural and experimental faults.

4. SURFACE FRACTURE ENERGY FROM GEOLOGICAL OBSERVATIONS

Seismogenic faults are nonplanar and exhibit geometrical, structural, and lithological variations that generate heterogeneous distributions of fault strength, initial shear stress (i.e., prestress τ_0), and resistance to seismic rupture and slip (Abercrombie et al. 2006, Faulkner et al. 2003, Fondriest et al. 2020, Masoch et al. 2021, Smith et al. 2013). Here we discuss the constraints to fracture energy estimates resulting from geological observations of fault zones (**Figure 2**). We discuss (*a*) the role of the DZ as an energy sink for a propagating seismic rupture within the FC (Section 4.1), (*b*) on-fault dissipation within the FC during seismic ruptures and slip (Section 4.2), and (*c*) rupture propagation on thin PSZs and their analog with sliding bare surfaces used in laboratory experiments (see also **Supplemental Text Sections 3** and **4**).

Supplemental Material >

4.1. Off-Fault Damage as Energy Sink (W_{off})

Earthquake ruptures dynamically activate off-fault damage around the FC (Dor et al. 2006, Fondriest et al. 2015, Mitchell & Faulkner 2009, Okubo et al. 2019). The width of DZs scales with displacement, fault length, crustal depth, and earthquake rupture velocity (Faulkner et al. 2011, Lyakhovsky 2001, Okubo et al. 2019, Savage & Brodsky 2011). Field data have been interpreted both as a process zone model of fault growth and as an increase in frictional displacement due to geometric irregularities, fault roughness, or prestress heterogeneity (Griffith et al. 2010, Tal & Faulkner 2022). The DZ contains intra- and intergranular microcracks, pulverized rocks, and mesoscale tensile and shear fractures; these structural features decrease exponentially with distance from the FC (Dor et al. 2006, Fondriest et al. 2020, Griffith et al. 2010, Mitchell & Faulkner 2009, Rockwell et al. 2009, Scholz et al. 1993, Vermilye & Scholz 1998, Wilson et al. 2005). This implies that mechanical (e.g., trapped waves, wrinkle-like pulses, fracturing and formation of Riedel-type shears, grain impingement) and possibly thermal (e.g., thermal cracking) processes acting at different scales coexist and produce off-fault damage (Andrews & Ben-Zion 1997, Ben-Zion 2001, Ben-Zion & Sammis 2013, Dor et al. 2006, Passelègue et al. 2016b, Tal & Faulkner 2022). Furthermore, geological observations are explained in terms of plastic strain processes caused by both the stress concentration in the zone around the advancing rupture front and anelastic strain caused by stress perturbations within a broader slipping zone, after the passage of the rupture front. This might also suggest that in natural faults the energy necessary to sustain the rupture propagation is defined not solely by the on-fault energy flux at the crack tip but also along a broader volume (Ben-Zion & Sammis 2013, Passelègue et al. 2016b) (see **Supplemental Figure 3.1**).

Geological estimates of W_{off} are mainly based on the measure of the micro- (which contribute the most to W_{off}) to mesoscale fracture surfaces (m^2) multiplied by the specific surface energy γ

[~1 J/m^2 for most minerals (Brace & Walsh 1962)] and normalized by unit fault area (Chester et al. 2005, Johnson et al. 2021, Pittarello et al. 2008). This results in the determination of a W_{off} that corresponds to a surface fracture energy per unit fault area (J/m^2). The geological estimates of energy loss off-fault are quite scattered, ranging between 10^{-1} MJ/m^2 and 10^1 MJ/m^2 (Chester et al. 2005, Johnson et al. 2021, Ma et al. 2006, Pittarello et al. 2008, and references therein). This large variability is explained at least by (*a*) uncertainties in distinguishing on-fault and off-fault materials, (*b*) characteristics of the studied fault zone (wall rock lithology, cumulative fault displacement, fault exhumation depth, maximum magnitude of the earthquake, etc.), (*c*) the poor relation between fault zone cumulative damage and the one associated with individual seismic ruptures, (*d*) several not seismic-related damaging processes such as formation of drag folds, or (*e*) postseismic healing and sealing that may obliterate pristine coseismic features. Nevertheless, geological observations of damage patterns are used in numerical models to provide estimates of W_{off} and constrain their variability (Di Toro et al. 2005a, Okubo et al. 2019) (Section 5).

4.2. Energy Dissipation in the Fault Core (W_{on})

The mechanisms involved in the on-fault (PSZs and FC, **Figure 2**) energy dissipation are diverse, and their relevance depends on the adopted fault zone model. For instance, the identification of the slipping zone during the earthquake rupture depends on the rheology and the strain rate characterizing the FC. Moreover, several proposed coseismic dynamic weakening mechanisms such as frictional melting (Nielsen et al. 2008), pore fluid thermal pressurization (Bizzarri & Cocco 2006, Lachenbruch & Sass 1980, Rice 2006, Wibberley & Shimamoto 2005), elastohydrodynamic lubrication (Brodsky & Kanamori 2001, Cornelio et al. 2019), or grain size and temperature-dependent viscous mechanisms (De Paola et al. 2015; Demurtas et al. 2019; Green et al. 2015; Nielsen et al. 2021b; Pozzi et al. 2018, 2019; Spagnuolo et al. 2015) require that the PSZ has a specific thickness (as illustrated in **Supplemental Figure 3.1**).

Grain size reduction and formation of nanoparticles and amorphous materials are attributed to mechanical and thermal processes associated with rupture propagation and seismic slip (Billi & Storti 2004, Ohl et al. 2020, Pec et al. 2012, Sammis et al. 1987, Siman-Tov et al. 2013, Storti et al. 2003). Wear and comminution by rupture propagation and shear in bare surfaces or within gouge layers cause grain size reduction and mechanical amorphization due to high stresses concentration at grain contacts (Rabinowicz 1966, Sammis & King 2007, Sammis et al. 1987, Storti et al. 2003). Transient heat pulses associated with coseismic frictional sliding result in mineral breakdown due to (*a*) dehydration and decarbonation of clays, serpentine, calcite, dolomite, etc.; (*b*) thermal expansion of rock-forming minerals; and (*c*) decrepitation of fluid inclusions hosted in the minerals (Collettini et al. 2013, Demurtas et al. 2016, Sibson 1975).

Similarly, as for the estimate of surface energy in DZs (Section 4.1), the estimate of the energy dissipated in the formation of new grain surfaces in the FC requires the determination of grain size distributions and of the surface area of fine-grained materials (Chester et al. 2005, Ma et al. 2006, Pittarello et al. 2008). These measurements are susceptible to large errors, making the estimates of surface energy densities quite uncertain. In fact, the fragmentation of rocks in the FC is the result of hundreds to thousands of seismic ruptures plus postseismic slip episodes. As a consequence, the contribution of individual seismic ruptures in gouge formation may require strong assumptions (e.g., number of earthquakes). Also, the number of fine particles produced during seismic rupture propagation and slip, which mostly contribute to the surface energy estimate, might be drastically reduced by static recrystallization related to high-temperature annealing a few seconds after seismic slip arrest or by aggregation or dissolution processes during long-lasting postseismic deformation (e.g., pressure-solution processes) (Chester et al. 2005, Gregg 1983, Pittarello et al. 2008). In any case, for paleo-earthquakes estimated in the range of M_w 6–7, Chester et al. (2005)

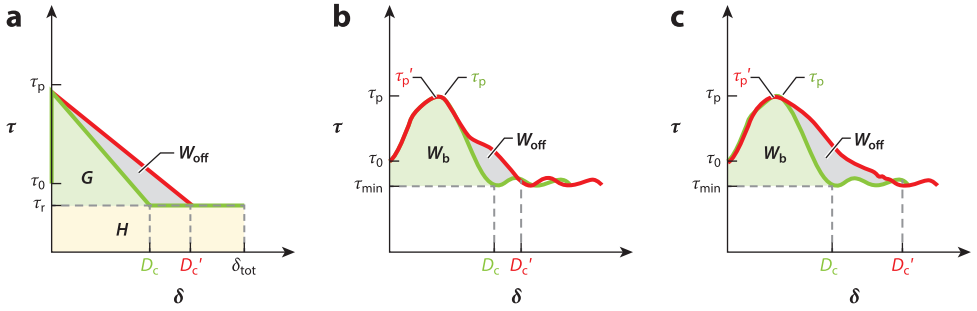

Figure 5

Effects of off-fault damage on dynamic weakening. The work density loss off-fault (W_{off}) is shown in gray. (*a*) The increase of fracture energy G and D_c due to off-fault damage for the Ida (1972) slip-weakening model (Okubo et al. 2019). The area below the residual stress labeled H identifies frictional heat ($\tau_r \delta_{tot}$). (*b*,*c*) The energy density loss off-fault for a generic shear stress evolution with slip. The peak shear stress τ_p (associated with the slip-weakening distance D_c; *green in color curve*) might be modified to τ_p' (associated with the increased slip-weakening distance D_c'; *red in color curve*) because of off-fault damage energy dissipation. In panel *b*, energy is dissipated off-fault when dynamic weakening is already started. In panel *c*, energy is dissipated off-fault when dynamic weakening initiates.

estimated a surface fracture energy density of $\approx 7\ 10^4$ J/m^2 (Punchbowl fault, California), and Pittarello et al. (2008) estimated a value of $\approx 85\ 10^4$ J/m^2 (for a single ancient earthquake, Gole Larghe fault, Italy). Instead, Ma et al. (2006) estimated a surface energy density $\approx 65\ 10^4$ J/m^2 for the 1999 Chi-Chi earthquake (Chelungpu fault, Taiwan). Given that the W_b estimates for earthquakes of this magnitude are up to 80 10^6 MJ/m^2, only 1–10% of breakdown work went into the formation of new grain surfaces (Cocco et al. 2006, Pittarello et al. 2008). Clearly, the energy sink associated with geological surface fracture energy can lie anywhere below the slip-weakening curve (**Figure 4**), also during dynamic fault weakening (Reches & Dewers 2005).

Frictional heat, defined as the portion of the energy below the residual shear stress level in Ida's (1972) slip-weakening law, is possibly the largest portion of the frictional work (Equation 3; **Figure 5*a***). Cocco et al. (2006) argued that this interpretation is model dependent, and that in a real fault the transition between heat and fracture or surface energy is not necessarily defined by the minimum or residual stress level. Frictional heat is certainly determined by frictional dissipation when sliding occurs at the dynamic friction level (given by the dynamic friction coefficient $\mu_d = \tau_r/\sigma_n$). However, depending on the thickness of the slipping zone, the largest increase of temperature occurs before and during dynamic weakening (Aretusini et al. 2021b; Cornelio et al. 2022; Nielsen et al. 2008, 2016b; and references therein). Despite this ambiguity, it is commonly accepted that frictional heat represents a high percentage ranging between 65% and 95% of the frictional work dissipated during dynamic rupture and arrest (Fulton & Rathbun 2011, Okubo & Dieterich 1984, Okubo et al. 2019).

The expression of the macroscopic frictional work given in Equation 4 can be applied to a thick fault zone shown in **Figure 2*b*** provided that the shear stress and slip are measured at the shear zone boundaries and that the thickness is constant during the coseismic phase. If the thickness changes during sliding, a further term is needed in measuring the frictional work density accounting for the work due to slip-induced dilation or compaction and depending on normal stress changes during sliding (Fulton & Rathbun 2011). It is worth of mentioning here that most of the discussions in the literature rely on the assumption that normal stress and fault zone thickness (and permeability) do not change during seismic sliding. However, these assumptions are often at odds with experimental evidence (e.g., Aretusini et al. 2021a).

4.3. Thin Principal Slipping Zones as Bare Surfaces

Geological observations also comprise evidence of ultracataclastic shear zones (usually less than 100 mm thick) within the FC including extremely thin PSZs, often much less than 1 mm thick (e.g., Chester & Chester 1998, Demurtas et al. 2016), limited by ultrapolished fault surfaces [fault mirrors (Fondriest et al. 2013, Siman-Tov et al. 2013)]. These thin PSZs and ultrapolished fault surfaces are the proxy of laboratory experiments conducted on saw-cut samples or bare surfaces to study fault friction and to propose constitutive friction laws (Dieterich 1979, Marone 1998). In fact, thin PSZs have specific contact properties and rupture surface topography, which are assumed to control friction during sliding (Dieterich 1979). Frictional contacts at the microscale or asperities have been evoked to propose coseismic dynamic weakening mechanisms, such as flash heating (Archard 1959, Goldsby & Tullis 2011). This simplified fault model is presented here because it is used in laboratory experiments and to interpret fault and dynamic weakening models relying on several constitutive parameters (e.g., slip or slip velocity and temperature) (Section 7). We anticipate here that, even in this apparently simple fault model, multiple processes occurring at different scales can explain dynamic fault weakening (Cornelio et al. 2022) (Section 7), thus contributing to the breakdown work dissipated during the coseismic phase.

5. ENERGY DISSIPATED IN THE DAMAGE ZONE (W_{off})

In Section 4.1 we reported the geological evidence of extended fault DZs. Theoretical, numerical, and experimental studies show that dynamic rupture propagation on planar and rough faults can generate a large amount of damage near faults (Andrews 2005; Ben-Zion & Ampuero 2009; Dunham et al. 2011a,b; Mia et al. 2022; Okubo et al. 2019; among many others). The numerical modeling of off-fault damage distribution around FCs using elastic-plastic off-fault materials has provided interpretative frameworks of the role of off-fault damages on the earthquake energy budget and fracture energy.

Andrews (2005) performed 2D nonelastic dynamic calculations of a thin planar fault surrounded by a DZ and demonstrated that the energy loss in the fault DZ contributes to the fracture energy that determines the rupture velocity of an earthquake. Off-fault material is subject to a Coulomb yield condition, and plastic strain is distributed along the fault and has a thickness depending on crack propagation distance. According to the model, the passage of the coseismic rupture front will leave behind it a wake of damaged rocks off the fault plane. This crack-like dynamic solution implies that energy dissipated off-fault is proportional to rupture propagation distance and is self-similar—that is, solutions at different times are related by scaling length in proportion to time. According to Andrews's calculations, the fracture energy and the slip-weakening distance D_c scale with rupture propagation distance, while peak slip velocity is proportional to the strength of the material. Thus, only the latter is a constitutive property. The energy density loss in the DZ can become a large fraction (≈80%) of the fracture energy prescribed in the constitutive law adopted to simulate the dynamic rupture propagation (Andrews 2005, figure 7).

Rice et al. (2005) performed 2D dynamic calculations for a fault governed by slip weakening and a self-healing pulse propagating dynamically in a steady-state configuration. The off-fault stress field is calculated from a propagating slipping zone (including the breakdown zone R as shown in **Figure 3**) behind the crack tip moving at constant rupture speed. This model assumes slip velocity pulses with both a rupture and a healing front, and a slip-weakening zone is imposed in the friction to remove the stress singularity at the rupture tip (Broberg 1978, Freund 1979, Nielsen & Madariaga 2003). The slipping patch propagates at constant rupture velocity, and the model allows computing the off-fault stress. This model predicts fracture energy scaling with total

slip in the event. Both Andrews (2005) and Rice et al. (2005) analyzed off-fault stressing near a nonsingular crack governed by a slip-weakening constitutive law. Their results confirm that energy density dissipated off-fault during the propagation of a crack or a pulse affects the fracture energy dissipated in the propagation of the rupture front.

Okubo et al. (2019) performed numerical modeling to study the mechanisms of coseismic off-fault fracturing and their effects on rupture dynamics. They found that off-fault damage decreases with rupture velocity (Biegel et al. 2008), limits peak slip velocity (Andrews 2005), and generates high-frequency radiation in the near-field. Okubo et al. (2019) showed that the fraction of fracture energy associated with off-fault damage increases with rupture length (20% variability) and depth (10% variability) and that fracture energy dissipated off-fault is 4% to 50% of the fracture energy dissipated on-fault.

Following Andrews (2005) and Okubo et al. (2019), it is appropriate to include the energy dissipated off-fault as a fraction of the total fracture energy G_{tot}, defined as (**Figure 5**)

$$G_{tot} = W_b^{tot} = G + W_{off}, \quad 9.$$

controlling the dynamics of rupture front propagation and its speed. In other words, fracture energy is dissipated in a volume around the rupture tip (**Figure 3**) and may therefore include an off-fault component W_{off} in addition to the component G dissipated on-fault (Aben et al. 2020). This means that off-fault plasticity and damage affect shear stress evolution and dynamic weakening (**Figure 5**), influence slip and rupture velocity, and might also further explain stress heterogeneity (Griffith et al. 2010) and rupture arrest (Mia et al. 2022). Equation 9 further corroborates the identification of the energy density dissipated off-fault in the DZ as an energy sink for the energy dissipated by the seismic rupture propagation.

The estimates of W_{off} from numerical modeling reveal a considerable variability in terms of both absolute values of energy density and the ratio with the fracture energy (W_{off}/G). The ratio between energy density dissipated off-fault and fracture energy (W_{off}/G) ranges between 1% and 50%. These modeling attempts indicate that, even when off-fault dissipation is a small fraction of total energy consumption, its impact on dynamic rupture process and stress heterogeneity is relevant and cannot be neglected.

6. FRACTURE ENERGY FROM SEISMOLOGICAL OBSERVATIONS

Our understanding of the dynamics of earthquake ruptures on natural faults is largely based on estimates of earthquake source parameters, such as stress drop, source dimension, rupture velocity, and slip as well as radiated seismic energy from seismological data (Abercrombie 2021, and references therein). These parameters can be inferred by modeling seismological data in different frequency ranges and considering the seismic source as a point source or an extended fault. Investigating the rupture process and source dynamics allows us to also estimate fracture energy and breakdown work for earthquakes in different magnitude ranges. In the following section we briefly discuss several approaches proposed in the literature to constrain these energy densities and discuss their scaling with earthquake size and implications on the energy budget, emphasizing that radiated seismic energy cannot be mapped on an extended fault (Kanamori & Rivera 2006).

6.1. Seismological Fracture Energy (G') from Point-Source Models

Abercrombie (2021) and Abercrombie & Rice (2005) describe the formulation of the earthquake energy budget for a point source relying on the widely adopted, simplified model in which the frictional work is partitioned in frictional heat and fracture energy (as illustrated in

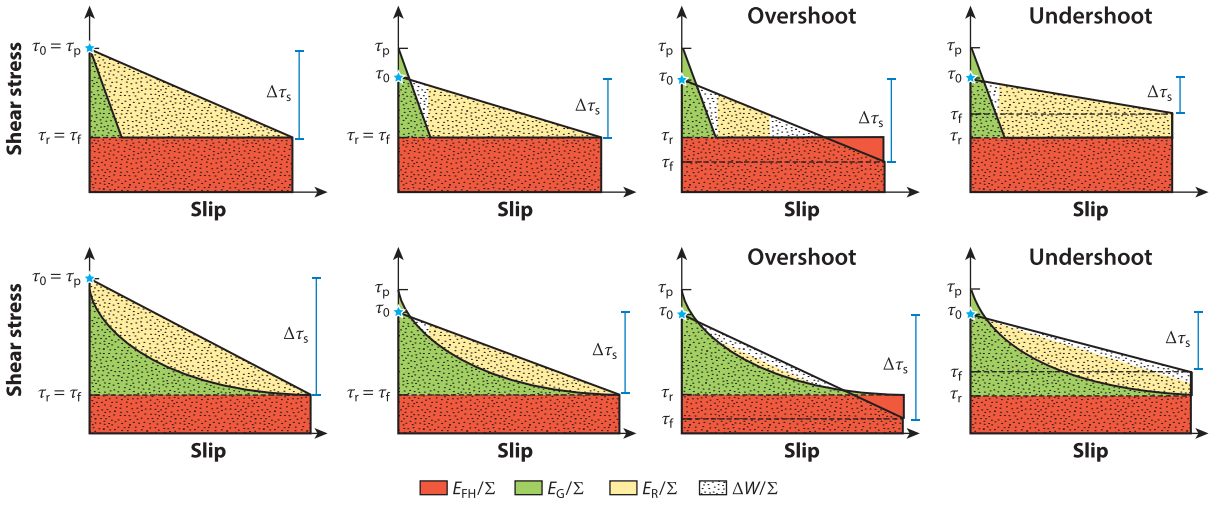

Figure 6

Examples of point-source representations of earthquake energy budget through the shear stress evolution with slip: linear slip-weakening models (*top panels*) and power-law models (*bottom panels*). Earthquake energy budget per unit rupture area is displayed by colored areas. Per unit rupture area, the total strain energy (*dotted overlay*) is partitioned into fracture energy (*green*), frictional heat (*red*), and radiated energy (*gold*). In the first column the initial stress is equal to peak stress ($\tau_o = \tau_p$) [i.e., strength excess ($\tau_p - \tau_o$) is zero], residual stress is equal to final stress ($\tau_r = \tau_f$) , and static stress drop $\Delta\tau_s = (\tau_o - \tau_f)$ is equal to dynamic stress drop $\Delta\tau_d = (\tau_o - \tau_r)$. In the second column, the shear stress is assumed to increase from an initial stress to peak stress with no slip ($\tau_o < \tau_p$). The third and fourth columns illustrate the overshoot ($\tau_r > \tau_f$) and the undershoot ($\tau_r < \tau_f$) models, respectively (as a consequence, $\Delta\tau_s \neq \Delta\tau_d$). The additional dissipation outside of the hatched trapezoid, associated with the strength excess ($\tau_o < \tau_p$) or with the overshoot condition, comes at the expense of the radiated energy. In these examples the gold area is drawn only as a sketch to represent geometrically a correct energy balance and has no relation with time and slip. The blue star individuates τ_o.

Figures 5*a* and **6**),

$$\Delta W = E_R + (E_{FH} + E_G) \quad (\text{in Joule}), \tag{10.}$$

where ΔW is the total (elastic and gravitational) strain energy variation at the source, E_R is the radiated energy, E_{FH} is the frictional energy (heat) dissipated during frictional sliding (**Figure 6**), and E_G is the total fracture energy. In this model, $E_{FH} + E_G$ corresponds to the energy dissipated within the fault zone (E_{FZ} in Equation 1).

Knopoff (1958) assumed that ΔW is equivalent to $\bar{\sigma}\,\Sigma\delta_{tot}$, where $\bar{\sigma} = (\tau_0 + \tau_f)/2$ is the average of the static stresses before and after the event, Σ is the total area of the event, and δ_{tot} is the final average slip. Indeed, ΔW can rarely be deduced from the radiated wavefield because single event recordings contain no information on the ambient stress (Beeler 2006). If the final stress τ_f is equal to the residual stress τ_r (no overshoot and undershoot), $E_{FH} = \tau_f \Sigma\delta_{tot}$ and then from Equation 10 the total fracture energy results are

$$E_G = \frac{\tau_0 + \tau_f}{2}\Sigma\delta_{tot} - \tau_f\Sigma\delta_{tot} - E_R = \frac{1}{2}\Delta\tau_s\Sigma\delta_{tot} - E_R, \tag{11.}$$

where $\Delta\tau_s$ is the static stress drop ($\tau_o - \tau_f$). Abercrombie & Rice (2005) propose the following relation to compute the so-called seismological fracture energy G′ from seismological data:

$$\frac{E_G}{\Sigma} = G' = \left(\frac{\Delta\tau_s}{2} - \sigma_a\right)\delta_{tot} \quad (\text{in Joule/m}^2). \tag{12.}$$

Equation 12 is obtained from Equation 11 introducing the apparent stress σ_a as (see Abercrombie 2021, and references therein)

$$\sigma_a = \mu \frac{E_R}{M_o},$$

where μ is rock rigidity (usually assumed as 30 GPa) and M_o is the seismic moment $M_o = \mu \Sigma \delta_{tot}$. G' from Equation 12 is an energy density (J/m^2). Seismological analyses allow the determination of radiated seismic energy from far field waveforms, seismic moment from moment tensors, and source dimension r from corner frequencies (Abercrombie 2021). The stress drop $\Delta\tau_s$ is often computed from the Brune (1970) relation

$$\Delta\sigma = C \frac{M_o}{r^3}, \qquad 13.$$

where r is the source radius (equivalent source dimension) and C is a constant depending on the source parameterization and geometry of the rupture area (Brune 1970, Madariaga 1978). According to these model-dependent assumptions, δ_{tot} is measured from seismic moment, being the fault area estimated from the equivalent source radius, stress drop from Equation 13, and apparent stress from radiated energy.

The assumption of a point-source model allows the graphic representation of the three terms in Equation 10 divided by fault area Σ on a single sketch as illustrated in **Figure 6**, which includes E_R because it represents the whole radiated energy from the source (Kanamori & Rivera 2006). **Figure 6** shows two simple models proposed to describe dynamic weakening and the earthquake rupture process for a point source: (*a*) a linear slip-weakening law (top panels) and (*b*) a power law (bottom panels). Seismological fracture energy G' is measured through Equation 12, which depends on the value of the final stress (τ_f). The original Ida (1972) slip-weakening model assumes that $\tau_f = \tau_r$ and that shear stress increases from initial to peak stress with no slip. The final stress τ_f can be smaller than the residual stress as in the overshoot model (Kostrov & Das 1988) or larger than the residual stress as predicted by the undershoot model (**Figure 6** third and fourth columns, respectively). The overshoot model is explained by inertial, propagation, and arrest effects (Beeler 2006) and can be generated by crack-like ruptures, while the undershoot model is predicted by healing of slip and slip pulse propagation (Heaton 1990). Radiated energy plotted in these sketches depends on both initial and final stress values. Panels in the first column of **Figure 6** show the case in which the initial stress is equal to peak stress ($\tau_o = \tau_p$), while the other panels show the case in which the initial stress is lower than peak stress. Because stress and slip are not uniform on a fault, the values used for a point-source model are averages over the fault during each seismic event. The graphs in **Figure 6** are drawn under the assumption that fracture energy (green area) is the energy dissipated in excess of frictional heat (red area) generated by slipping at the residual stress (see Section 4.2).

Computing G' with Equation 12 does not account for the dynamic weakening behavior because fracture energy is not computed from shear stress evolution but just considers the initial and final stress values. G' represents exactly the green area in **Figure 6** only when there is no under- or overshoot (first and second columns).

Notwithstanding, Equation 12 is applied to earthquakes in a wide range of magnitudes ($1 < M < 7$). The resulting values of G' range between 10^2 J/m^2 and 10^7 J/m^2 and increase with seismic slip (see also Abercrombie & Rice 2005, Malagnini et al. 2014, Rice et al. 2005, Selvadurai 2019, among many others) (**Figure 7**). **Figure 7** also includes G' values estimated by Viesca & Garagash (2015) for subduction zone earthquakes, which are slightly lower than those for regular earthquakes in the same slip range. These authors interpret this underestimate in terms of significant stress undershoot and reduced radiation efficiency of tsunamigenic earthquakes.

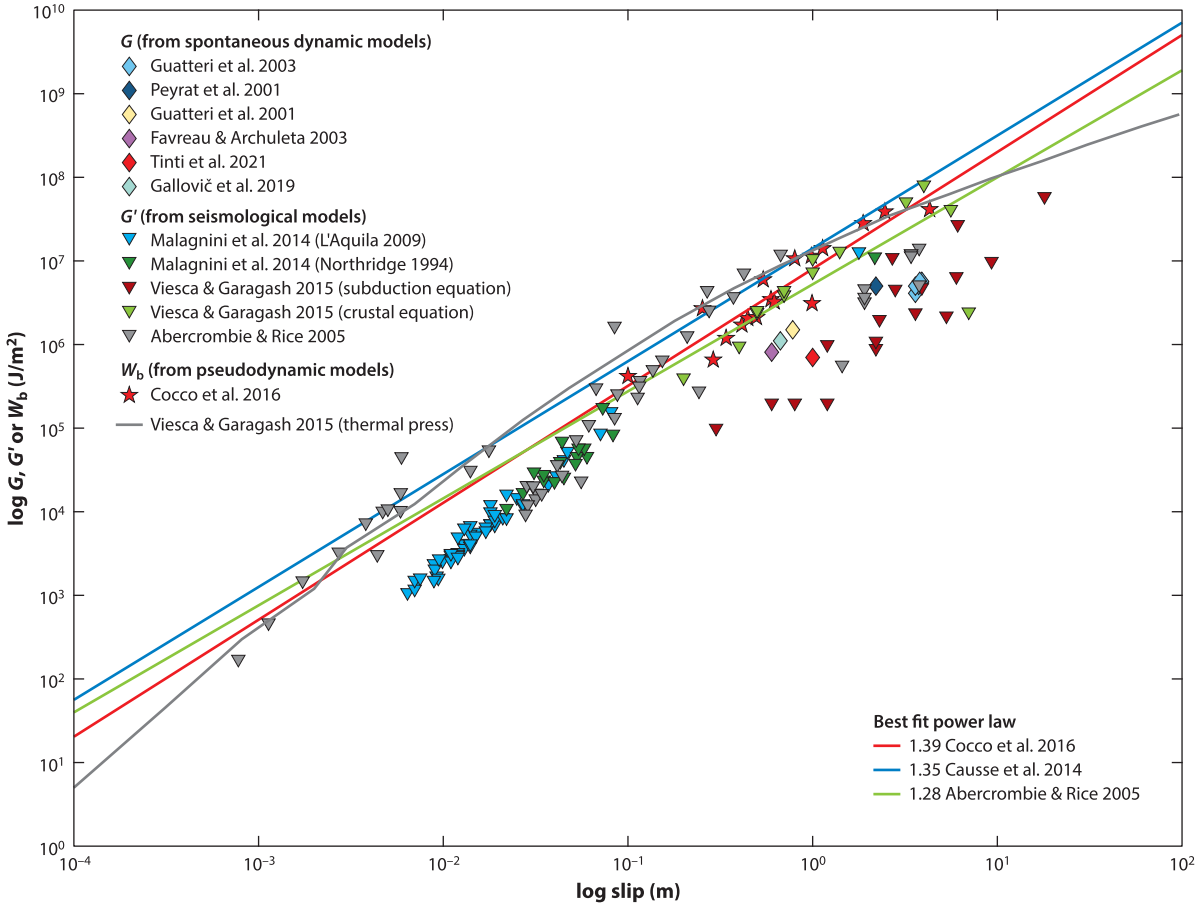

Figure 7

Scaling of average estimates of fracture energy and breakdown work with average slip.

These conditions of undershoot or overshoot significantly change the value of strain energy variation and consequently make the value of G' a minimum or a maximum (respectively) value of G (depicted as the green area in **Figure 6**). The scale dependence of seismological fracture energy has been interpreted as evidence that D_c also scales with total slip (see Equation 8) (Abercrombie & Rice 2005, Ohnaka 2013) as well as that G' includes further processes at different spatial and temporal scales triggered at different slip velocities and earthquake size (Brantut & Viesca 2017, Viesca & Garagash 2015) (see Section 8).

6.2. Fracture Energy G and Breakdown Work W_b from Extended Source Models

The rupture process on an extended fault is usually retrieved by inverting seismological and geodetic data through kinematic models or by modeling dynamic spontaneous propagation of coseismic ruptures on a prescribed fault. Kinematic source models provide the distribution of slip and rupture times on the assumed fault plane and image rupture velocity. Usually, they rely on matching seismological waveforms up to 1 Hz, and source models from recent earthquakes are available through a repository accessible from a dedicated webpage (Mai & Thingbaijam

2014). The spontaneous dynamic rupture models rely on assuming a constitutive slip-weakening or rate- and state-dependent law. For a slip-weakening law, for instance, it is necessary to adopt a spatial distribution of initial stress as well as to prescribe the peak and residual stress values and D_c to spontaneously propagate the rupture. The slip and rupture time distributions on the fault are obtained from the dynamic simulations. More recently, several authors have constrained spontaneous dynamic rupture models fitting seismological data at frequency less than 5 Hz and inverting for the dynamic parameters. Most of them assume the Ida (1972) linear slip-weakening law (Favreau & Archuleta 2003; Gallovič et al. 2019, 2020; Guatteri & Spudich 2000; Guatteri et al. 2003; Peyrat et al. 2001; Tinti et al. 2021) and fracture energy are measured from constrained dynamic parameters as the energy in excess to frictional heat. Values of fracture energy from dynamic spontaneous modeling of an earthquake rupture propagation on a finite fault are shown in **Figure 7** and compared with other seismological estimates.

Shear stress evolution during coseismic ruptures can be inferred through pseudodynamic modeling where the rupture front propagation, source time function, and other kinematic features are prescribed (Bouchon 1997; Causse et al. 2014; Ide & Takeo 1997; Mai et al. 2006; Tinti et al. 2005a,b). Tinti et al. (2005b) estimated breakdown work (Equation 5) on extended faults for several earthquakes by retrieving dynamic stress evolution at each point on the fault plane from slip history imaged by inverting ground motion waveforms. These authors used a 3D finite difference algorithm to compute the dynamic traction evolution in the time domain during the earthquake rupture from the elastodynamic equation proposed by Fukuyama & Madariaga (1998). The shear stress evolution with time and slip can be retrieved in different patches on the fault plane (Bouchon 1997, Causse et al. 2014, Ide & Takeo 1997, Tinti et al. 2009) as shown in **Supplemental Text Section 2** and **Supplemental Figure 2.1**.

Supplemental Material >

Tinti et al. (2005b) proposed to estimate W_b by calculating the scalar product between dynamic traction and slip velocity vectors. Average estimates of W_b can be calculated considering the whole fault plane or fault patches where the slip is larger than a predefined threshold [a percentage of maximum or average slip (see Cocco & Tinti 2008, Cocco et al. 2016)]. In fact, Guatteri & Spudich (2000) demonstrated that D_c cannot be measured from stress evolution curves because there is a trade-off between dynamic parameters, but G or W_b estimates are better constrained. So different values of D_c and breakdown stress drop can equally fit the data, while G or W_b can be retrieved. Kinematic models assume a slip velocity pulse as source time function (Tinti et al. 2005a), and this explains why the final stress is larger than the minimum stress in many positions on the extended fault as an undershoot model (**Supplemental Figure 2.1**).

In general, it is not possible to assess a priori whether dynamic parameters derived from pseudodynamic modeling can propagate spontaneously and therefore define a priori the energy necessary to propagate the rupture. The uncertainty in W_b estimates for large events based on finite-fault kinematic inversions may stem from nonuniqueness of finite source inversion for a given event, as well as from different sets of assumptions (e.g., smoothing, interpolation) involved with modeling coseismic stress changes based on a given fault slip kinematics (Viesca & Garagash 2015). However, it has been shown that the uncertainties in energy density estimates can be roughly constrained to a factor of two (Causse et al. 2014, Guatteri & Spudich 2000).

Tinti et al. (2005b) and Cocco et al. (2006) discussed the distributions of breakdown work density for numerous earthquakes and concluded that breakdown work scales with slip. They found that for an individual earthquake, the scaling of breakdown work with slip for all the points on the assumed fault plane is expressed by $W_b \propto \delta_i^2$ (where δ_i is the slip in the i-th cell of the discretized fault plane) in agreement with the theoretical model by Rice et al. (2005), except for models with supershear ruptures where the scaling relation can be more complex (Cocco et al. 2016). Furthermore, Cocco et al. (2016) concluded that the scaling of average estimates of breakdown work with

slip for individual earthquakes follows a different power law. This requires representing breakdown work and slip with a single number for each earthquake rupture and, therefore, implies averaging on the fault plane.

Figure 7 reports the scaling, for recent earthquakes, of breakdown work W_b (stars) with average final slip. Different energy estimates (G, G', W_b) are used in this figure as indicated by the symbols, and the proposed scaling relations are obtained for values computed by averaging on the whole fault plane. Tinti et al. (2005b) and Cocco et al. (2016) have shown that the inferred scaling ($W_b \propto \delta^{1.4}$) agrees with Causse et al. (2014) ($W_b \propto \delta^{1:35}$) and Abercrombie & Rice (2005) ($G \propto \delta^{1.28}$). Moreover, Cocco et al. (2016) emphasized that adopting different spatial averages on the fault plane affects the scaling of breakdown work (the slope of the regression with slip ranges between 1.4 and 2.0). These authors concluded that breakdown work increases with earthquake size, even if the slope of the regression is slightly higher (1.4) than that inferred by Abercrombie & Rice (2005) and Nielsen et al. (2016a,b) (1.28) but smaller than that inferred by Viesca & Garagash (2015) for small- to moderate-magnitude earthquakes (2.0). The differences in the slope of the regression might depend on the adopted weighting for spatial averaging. Notwithstanding this modest variability, and despite the differences between the methodologies and the assumptions implicit in the modeling, models yield similar G', G, and W_b values that consistently scale with seismic slip (**Figure 7**).

7. FRACTURE ENERGY FROM LABORATORY EXPERIMENTS

Earthquake mechanics has been widely investigated through dedicated rock deformation experiments (for reviews, see Abercrombie et al. 2006, Paterson & Wong 2005, Scholz 2019). With respect to natural faults, the main advantage is that experiments are performed under controlled conditions and the simulated fault can be monitored in real time. In fact, the shear stress, fault slip and slip velocity, strain, radiated elastic waves (i.e., acoustic emissions), elastic properties, temperature, and permeability are measured close to the experimental fault. Moreover, the experimental products can be recovered for microstructural and microanalytical studies to possibly infer the dynamic weakening mechanism and for comparison to natural fault products. Laboratory experiments require solving technical challenges to reproduce the complexity of natural faults. For example, the complex structure of natural faults and associated SZs (**Figure 2**) is often simplified in the laboratory using intact rocks or bare surfaces of rigid blocks [made of rock or analog materials such as polymethyl methacrylate (PMMA) glass] or noncohesive materials sandwiched in between (i.e., fault gouges) (see discussion in Section 4.3 and **Supplemental Figure 4.1**). Typical stress conditions (up to few GPa) and slip velocities (from nm/s to m/s) achieved on natural faults in Earth's crust are reproduced in the laboratory by combining non-, gas-, solid-, or oil-confined biaxial, triaxial, and rotary shear machines with different sample assemblages and dedicated sample holders (Paterson & Wong 2005) (see **Supplemental Text Section 4**). Forces and/or torques are transferred from the machine to the sample by controlling the advancement of the pistons (i.e., biaxial, triaxial machines) or the rotation of a column (i.e., rotary shear machines). Therefore, although with several limitations including the scaling to natural conditions, laboratory experiments can reproduce the complexity (structural and compositional heterogeneities, presence of fluids, etc.) of natural faults and fault materials as well as the main phases of the seismic cycle (**Figures 1** and **2**; **Supplemental Text Section 4**).

In this section, given that the earthquake rupture process includes both shear fracture and frictional sliding of rocks, we focus on experiments designed to measure fracture energy through three types of experimental configurations: (*a*) shear fracture of intact rocks, (*b*) stick-slip experiments, and (*c*) high-velocity friction experiments. Definitions of fracture energy and equations used by referenced authors are listed in a dedicated table in **Supplemental Text Section 5**.

Supplemental Material >

7.1. Fracture Energy in Shear Fracture of Intact Rock Experiments

A quantity measured using fracture of intact rock experiments is the (in-plane)[1] shear fracture energy G_{IIc} or critical energy release rate under mode II crack propagation. G_{IIc} is measured from the integration under the postfailure stress-slip curve (Wong 1982) (Equation 6; **Supplemental Figure 4.1*a***) and is a measure of the energy required to propagate a crack of a unit surface (Palmer & Rice 1973; Rice 1979). In triaxial experiments, sample failure occurs along a localized deformation zone oriented in most rocks at an angle of $15 \sim 45°$ with respect to maximum compression direction (e.g., Wong 1982), consistent with the location of acoustic emissions produced by the specimen (e.g., Lockner et al. 1991). Under typical upper crustal loading conditions, the experimental values of G_{IIc} for intact crystalline low-porosity rocks are of the order of $\sim 10^4$–10^5 J/m^2 [27 10^3 J/m^2 (Aben et al. 2019), 13–51 10^3 J/m^2 (Wong 1982, 1986), 13–29 10^3 J/m^2 (Lockner et al. 1991), 14–800 10^3 J/m^2 (Ohnaka 2003)] (**Figure 8**). The values of G_{IIc} of intact rocks (*a*) scale with slip distance δ according to the power law $G_{IIc} \propto \delta^{\alpha}$ with $\alpha \approx 1.11$ and (*b*), for a given δ, are larger than those measured with the other experimental configurations (**Figure 8**). In these experiments, the seismological G' (Section 6) was also estimated by measuring the seismic moment, the corner frequency, and the radiated energy obtained from the inversion of the acoustic waves (Sellers et al. 2003, Yoshimitsu et al. 2014). Additionally, off-fault damage fracture energy (W_{off}) can be measured using acoustic waves tomography in experiments with small δ (<1 mm) resulting in $W_{off} \approx 2$ to 10 kJ/m^2 (Aben et al. 2020). This estimate is close to the energy dissipated off-fault as established from the microstructural analysis of the new cracks produced in these experiments. Aben et al. (2019) report that W_{off}/G_{IIc} is ~10%, resulting in 90% of fracture energy being dissipated by on-fault processes.

7.2. Fracture Energy in Stick-Slip Experiments on Precut Specimens

In stick-slip frictional sliding experiments performed on precut specimens, G is measured from the shear stress versus slip curve either computing the integral as in Equation 5 (e.g., Ohnaka 2003, 2013) or using the initial and final stress values (e.g., Equation 7) (Lockner & Okubo 1983; Rice 1979). In this experimental configuration (**Supplemental Figure 4.1*b***), the values of G are systematically smaller than those of G_{IIc} measured for failure of intact rocks under similar loading conditions (Aubry et al. 2018; Beeler et al. 2012; Lockner & Okubo 1983; Ohnaka 2003; Okubo & Dieterich 1981, 1984; Passelègue et al. 2016a, 2017) (**Figure 8**; Section 7.1). The values of G for precut specimens scale with slip distance δ according to $G \propto \delta^{2.56}$ (Ohnaka 2003; Passelègue et al. 2016a, 2017) (**Figure 8**). Instead, in experiments performed in double-direct shear configuration on fault gouges (**Supplemental Figure 4.1*b***) and where slow-slip frictional instabilities where triggered, $G \propto \delta^{1.97}$ and $G \propto \delta^{1.76}$ for quartz and anhydrite/dolomite mixtures, respectively (Scuderi et al. 2020) (**Figure 8**).

Another method to compute the fracture energy is through the measurement of dynamic stresses over a short time window (10 to 100 μs) obtained by the installation of high-frequency strain gauges [up to 10 MHz (Passelègue et al. 2016a)] and calibrated acoustic transducers (Selvadurai & Glaser 2017) located close to the saw cut surface (1 mm). Dynamic stresses are used to estimate fracture energy from the integration of the near-fault stress-slip curve (Paglialunga et al. 2022, Passelègue et al. 2016a) and also by means of the LEFM and the cohesive zone models (Kammer & McLaskey 2019, Ke et al. 2018, Paglialunga et al. 2022) (Γ in **Figure 8**; **Supplemental Text Section 5**). These techniques have been employed both in triaxial tests on solid precut

[1] Sliding mode: shear stress is acting parallel to the plane of the crack and perpendicular to the crack front.

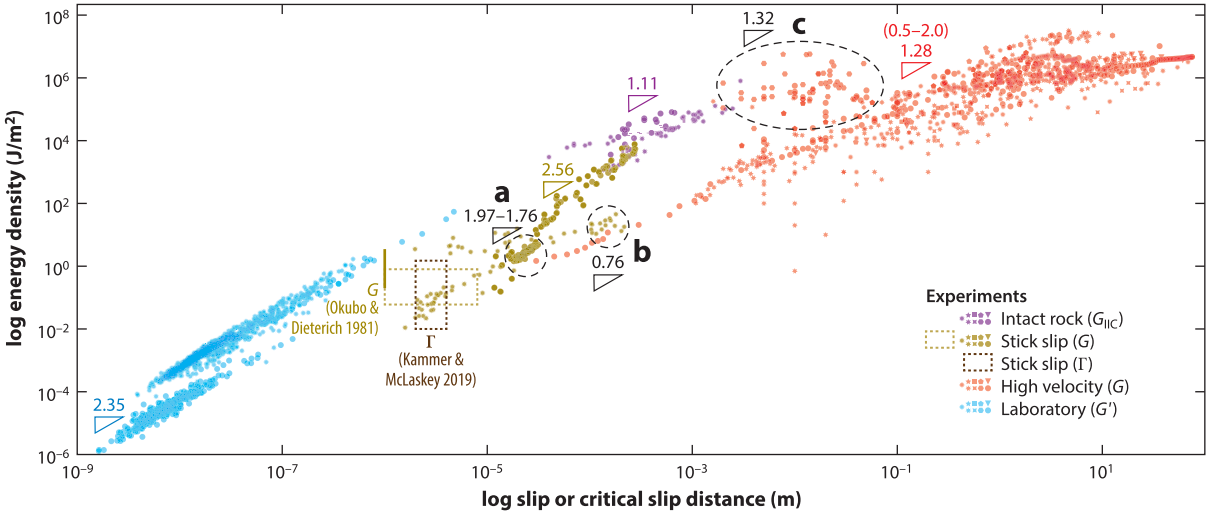

Figure 8

Fracture energy data from laboratory experiments (this data set can be downloaded from **https://doi.org/10.5281/zenodo.6833943**). Data are included either as points or as vertical lines to indicate variability in energy density, or as boxes to indicate variability of both energy density and slip. Energy density scales with slip distance according to the power law ($G_{\|C}$, G, Γ, G') $\propto \delta^{\alpha}$. The values of exponent α are reported close to each cluster of data points. We highlight three clusters of data with their respective exponent α: (*a*) from Scuderi et al. (2020), (*b*) from Paglialunga et al. (2022), and (*c*) from Chang et al. (2012) (see descriptions in the main text). Colors indicate distinct data sets divided in groups depending on the type of energy density and experimental configuration as follows: blue: estimates of G' by McLaskey et al. (2014), Sellers et al. (2003), Selvadurai (2019), and Yoshimitsu et al. (2014) (Sections 7.1 and 7.2); purple: estimates of G_{IIC} by Aben et al. (2019, 2020), Hakami & Stephansson (1990), Liu & Rummel (1990), Lockner et al. (1991), Moore & Lockner (1995), Ohnaka (2003), Ohnaka et al. (1997), Rummel et al. (1978), Wawersik & Brace (1971), and Wong (1982, 1986) (Section 7.1); yellow: estimates of *G* by Ohnaka (2003), Okubo & Dieterich (1981, 1984), Paglialunga et al. (2022), Passelègue et al. (2016a, 2017), and Scuderi et al. (2020) (Section 7.2); gold: estimates of Γ by Kammer & McLaskey (2019) and Ke et al. (2018) (Section 7.2); and red: estimates of *G* by Aretusini et al. (2021a), Boulton et al. (2017), Boutareaud et al. (2012), Brantut et al. (2008), Chen et al. (2017), Cornelio et al. (2019, 2020), De Paola et al. (2011), Del Gaudio et al. (2009), Di Toro et al. (2006, 2011), Faulkner et al. (2011), French et al. (2014), Han et al. (2007, 2010), Harbord et al. (2021), Hirose & Bystricky (2007), Hou et al. (2012), Mizoguchi et al. (2007), Nielsen et al. (2016a, 2008), Oohashi et al. (2015), Passelègue et al. (2016b), Rempe et al. (2017), Sawai et al. (2012, 2014), Seyler et al. (2020), Smith et al. (2013), Togo & Shimamoto (2012), Togo et al. (2011, 2016), Ujiie & Tsutsumi (2010), Ujiie et al. (2013), Vannucchi et al. (2017),Violay et al. (2013, 2014), and Yao et al. (2013) (Section 7.3).

surfaces (Passelègue et al. 2016a) and in biaxial experiments in direct shear configuration, using solid large precut rocks (Kammer & McLaskey 2019; Ke et al. 2018; McLaskey et al. 2014, 2015) and rock analogs (Bayart et al. 2016a, 2018; Paglialunga et al. 2022; Svetlizky & Fineberg 2014). Paglialunga et al. (2022), using PMMA, reported a dual-scale weakening: The first weakening stage (at the tip of the rupture front) provides energy density estimates that are independent from the fault displacement and are consistent with the estimates of energy densities from LEFM and cohesive zone models. The second weakening stage provides energy densities that scale with $\delta^{0.76}$ (**Figure 8**).

In experiments performed with host blocks made of transparent and photoelastic materials (i.e., Homalite), it is possible to observe the propagation of the rupture front and to measure the rupture velocity (Guérin-Marthe et al. 2019, Rosakis 2002). These experiments performed on rock-analog materials support the LEFM theory in earthquake modeling, but they do not fully represent the complexity of faults as observed in the field (see Section 4). In the stick-slip experiments, the seismological G' was estimated by measuring the seismic moment, the corner frequency, and the radiated energy obtained from the inversion of the acoustic waves

(McLaskey et al. 2014, Selvadurai 2019). These measures extend the range of slip displacement down to 10^{-9} m and yield $G' \propto \delta^{2.35}$ as reported in Selvadurai (2019).

7.3. Fracture Energy in High-Velocity Friction Experiments

High-velocity friction experiments reproduce the frictional power density ($\tau\dot{\delta}$) dissipated on a fault sheared at low normal stress (<50 MPa), but for slip typical of moderate- to large-magnitude earthquakes (up to tens of meters). The value of G is measured by integrating the shear stress-slip curve from either zero slip or the slip at the peak shear stress (e.g., D_a in Section 3) up to a reference distance D_w considered as the slip-weakening distance (D_c) (Equation 8; **Supplemental Figure 4.1*c***). In high-velocity friction experiments reproducing natural earthquakes, fracture energy scales with slip distance ($G \propto \delta^{\alpha}$ with $0.5 < \alpha < 1.3$), independently of rock composition, imposed normal stress and environmental conditions (presence/absence of fluids) (Cornelio et al. 2019, Nielsen et al. 2016a, Passelègue et al. 2016b, Violay et al. 2014). An exception is represented by experiments performed on phyllosilicate-rich gouges where the values of G are lower for similar slip distance and normal stress (Faulkner et al. 2011). However, the scaling between G and slip saturates at slip values larger than about 15 cm, which roughly corresponds to one rotation of the cylindrical sample (Nielsen et al. 2016a).

Supplemental Material >

The fracture energy G is also measured in spontaneous slip events triggered by the stepwise increase of shear stress in rotary shear unconventional experiments (Cornelio et al. 2020, Giacomel et al. 2018), resulting in $G \propto \delta^{1.02}$ (**Figure 8**). In other rotary shear experiments, abrupt slip pulses are imposed to the sample using a flywheel (Chang et al. 2012). These data scale as $G \propto \delta^{1.32}$ and form a cluster of points with higher fracture energy in the 0.001- to 0.1-m slip range (**Figure 8**).

8. DISCUSSION AND CONCLUDING REMARKS

This review addresses the issue of the energy dissipated in the fault zone during the propagation of a seismic rupture on a geological fault and contributes to the debate on the earthquake energy budget. Geological observations reveal that earthquakes nucleate, propagate, and arrest in complex fault zones (**Figure 2**) whose structural heterogeneity depends on the geometry, lithology, rheology, presence of fluids, and strain localization processes. The fault zone structure characterizes the response to tectonic loading and strain localization as revealed by the wide range of fault slip behaviors (e.g., creep, aseismic- and slow-slip events, afterslip, and earthquakes) occurring on a seismogenic fault. This implies that the environment in which earthquakes occur is diverse, and this explains why different physical and chemical processes can be involved in the coseismic dynamic rupture.

In this review we focused our attention on the dynamic rupture process following earthquake nucleation and terminating with rupture arrest. The failure at a point of a rupturing fault starts when stress from the initial level (τ_0) increases abruptly to τ_p, indicating the beginning of the coseismic phase (**Figure 1**). The dynamic weakening or breakdown stage, defined by the shear stress degradation from τ_p to a minimum (τ_{min}) value or residual (τ_r) level, characterizes the coseismic phase. The different processes governing dynamic weakening and rupture propagation act at different spatial scales, from the microscale of asperity contacts on bare surfaces, or fracture and slip of the fault gouge materials (**Supplemental Figure 3.1**), to the macroscale of the response of fault patches to the dynamic reduction of shear resistance. Geological observations show that fault zones have a variable thickness, and coseismic dynamic weakening processes can also occur at the mesoscale (bulk response). This implies that the rupture process on geological faults involves both fracture (mainly at the microscale) and friction (at the meso- and macroscale) (see **Supplemental Text Section 3**). In the literature, the earthquake dynamic rupture has been described in terms

of either fracture or frictional processes (Scholz 2019). We emphasize here that both processes can jointly affect dynamic weakening and coseismic rupture propagation and, more important, in both cases fracture energy is mathematically computed from the drop of shear stress on the fault as shown in Equations 5 and 8. Brittle failure involves both fracture and friction because frictional sliding along preexisting faults requires the breakage of asperities at various scales and the fracturing of previously healed fault segments (e.g., Brantut et al. 2013, Sibson 1986).

If coseismic slip represents the displacement field associated with the rupture extension, the shear stress evolution during the coseismic phase characterizes and describes the response of the fault to dynamic loading and contains all the available information on the energy dissipated during the rupture propagation. Because of the diversity of the geological conditions and the complexity of the rupture process involving many different physical and chemical processes, it is reasonable to expect that shear stress evolution during dynamic rupture is also diversified (e.g., **Figures 4** and **6**). The analytical dependence of shear stress from source parameters (e.g., slip, slip velocity, temperature, permeability) defines the constitutive law used to prescribe shear stress evolution during rupture propagation and to eliminate singularities at the crack tip. In this study, we represented shear stress evolution as a function of slip because this dependence is widely used (Ohnaka 2013, and references therein) and for its usefulness in determining the energy dissipated during dynamic propagation (Equations 5, 6, 8). This does not mean that shear stress depends only on slip, and slip should not be considered as a constitutive parameter. Shear stress evolution depends on many other parameters and variables, and its dependence on slip rate and temperature has been corroborated by a wealth of laboratory experiments in the last decades (Di Toro et al. 2021).

During the dynamic rupture, the shear stress at a given point on the fault changes with time from the initial to the final value, and this defines the rupture duration and determines the slip velocity time history (Tinti et al. 2005a, among many others). Shear stress evolution in space, when the rupture front is at a given point on a rupturing fault, is extremely important to discuss the dynamic weakening and the edge-localized dissipation. Here we propose that shear stress evolves from its initial value slightly ahead of the tip to the minimum or residual value at the end of the breakdown stage, and in agreement with Chen et al. (2021) we call this spatial range a rupture front zone, as shown in **Figure 3**. The size of the rupture front zone and the existence of a slipping zone behind it, as shown in **Figure 3**, depend on the existence of a constant residual stress independent of slip as predicted by classic slip-weakening laws (**Figure 4*a***). In this case, it is possible to identify a zone characterized by frictional sliding at the dynamic friction coefficient (μ_d) and distinguish between rupture and friction. However, if the shear stress evolution in the rupture front zone is characterized by a power-law decay (**Figure 4*d***), the constant residual stress does not exist because D_c might be equal to the final slip. We cannot exclude one of these two scenarios because of geological structural heterogeneity, experimental results (Ohnaka 2003), and dynamic modeling results (Brantut & Viesca 2017, Lambert & Lapusta 2020). In particular, Viesca & Garagash (2015) have shown that changing the thermal and the poroelastic conditions, shear stress evolution with slip changes between the two limiting configurations here described (**Figure 4*c*,*d***). Because we are using in this description macroscopic quantities, such as shear stress and coseismic slip, it is preferable to avoid denoting the processes occurring within the rupture front zone as fracture or friction. This implies that the size of the rupture front zone, corresponding to the zone of inelastic dissipation or edge-localized dissipation (Brener & Bouchbinder 2021), is finite, likely smaller than the rupture length, and it depends on dynamic weakening rate and therefore on breakdown stress drop and D_c (Fialko 2015).

A further consideration concerns the slip value D_a associated with the shear stress increase from the initial to the peak value. In Ida's (1972) slip-weakening law, $D_a = 0$ and the increase to the peak stress is linear (elastic and reversible), and this explains its application in the framework

of LEFM. Based on laboratory experiments, Ohnaka (2013, equation 3.18, p. 61) suggests that D_a is directly proportional to D_c and interprets this scaling in terms of frictional breakdown stress drop ($\Delta\tau_p/\tau_p$) and fault roughness. Here we recall that both breakdown work and fracture energy measured through Equations 5 and 8, respectively, include the work done in the slip range 0–D_a. If the shear stress evolution in this slip range is not linear, at least from the yield stress (τ_y) to the peak stress (τ_p), this work is irreversible and inelastic. It is possible to speculate that the work dissipated before dynamic weakening is driving slip acceleration near or ahead of the crack tip. The macroscopic definition of breakdown work (Equation 5) corresponds to the work spent on evolving the shear stress on a fault to a minimum level. This implies that in its general formulation breakdown work (Equation 5) and fracture energy (Equation 8) are equivalent, and they represent the energy dissipated in excess of a minimum or residual stress value. Here we still assume that the coseismic slip represents the displacement field associated with the rupture extension. The contribution of off-fault energy dissipation is not included.

Our review confirms that most of the work spent during an earthquake is consumed by dissipative processes occurring in complex fault zones, much larger than energy radiated as seismic waves (Udias et al. 2014). Geological observations provide evidence of the off-fault DZ interpreted in the literature as an energy sink for rupture propagation in the FC. Modeling results and experimental observations (Aben et al. 2019) show that a non-negligible portion of energy is dissipated off-fault in a volume around the rupture tip and that off-fault plasticity and damage affect shear stress evolution and dynamic weakening (as illustrated in **Figure 5**). The presence of off-fault damage can affect the spatial dimensions of the rupture front zone (Andrews 2005). This implies that fracture energy and D_c are not material properties and constitutive parameters. Furthermore, in addition to the fracture energy dissipated on-fault (Equation 9), there is an off-fault dissipation (W_{off}) affecting the dynamic rupture process and stress heterogeneity that cannot be neglected.

In this review we collected from available literature geological estimates of surface energy, seismological estimates of fracture energy G' from point-source models, breakdown work W_b from finite-fault models, fracture energy G from spontaneous dynamic models, and a wealth of fracture energy estimates using different approaches from very diverse laboratory experiments (**Supplemental Text Section 4**). This allowed us to compare the inferred fracture energy values and discuss their scaling with slip and earthquake size. Our analysis confirms that seismological estimates of fracture energy and breakdown work are comparable and scale with seismic slip (**Figure 7**). The inferred scaling laws show modest deviations explained in terms of epistemic uncertainties. The original collection of fracture energy estimates from laboratory experiments confirm the scaling with slip over a slip range of more than 10 decades (**Figure 8**). Fracture energy associated with breaking of intact rocks is larger than for precut specimens (Ohnaka & Shen 1999) and might suggest differences between the role of fracture and friction, or a different size of the rupture front zone. Finally, it is important to recall that fault products after deformation in the laboratory correspond to fault products observed in nature (Acosta et al. 2018, Di Toro et al. 2006), and acoustic emissions recorded in the laboratory can be processed as seismic waves on a natural fault (Selvadurai 2019).

Supplemental Material >

The merged data set composed of all the fracture energy (density or J/m^2) estimates collected in this study is shown in **Figure 9**. This figure shows that, within a relatively large dispersion, geological, laboratory, modeling, and seismological estimates of fracture energy scale with slip. The evidence that fracture energy estimated in the laboratory by analyzing acoustic emissions with seismological approaches scales consistently with seismological measures for real earthquakes corroborates the scaling with slip. This suggests that, even if poor resolution of seismological data might bias inferred fracture energies, they scale consistently with slip from the laboratory to the

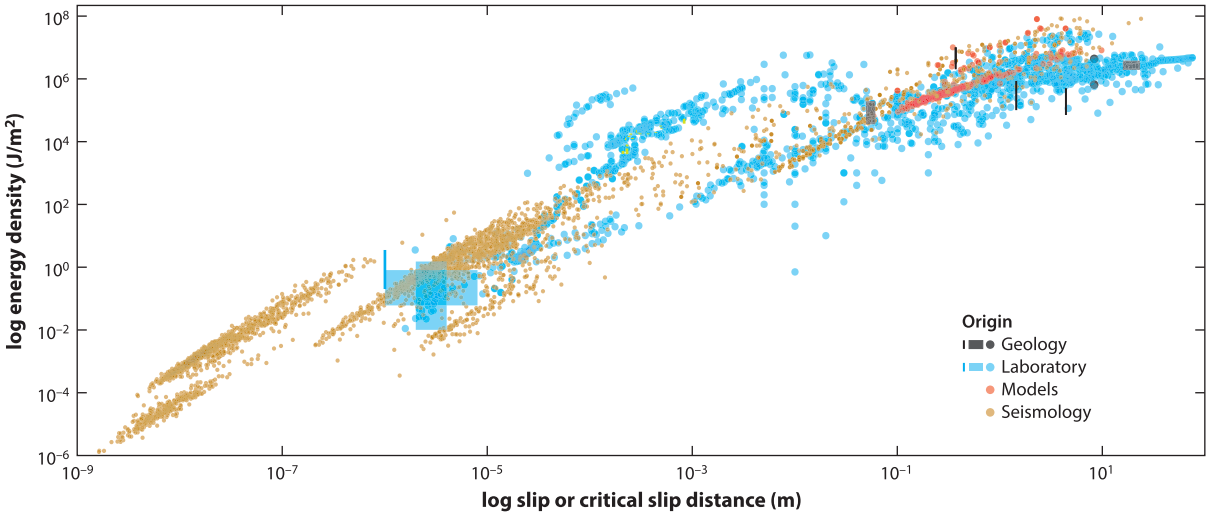

Figure 9

Scaling of fracture energy densities with slip associated with rupture propagation and slip estimated from geological (Section 4), seismological (Section 6), and laboratory (Section 7) studies. Data are included either as points or as vertical lines to indicate variability in energy density, or as boxes to indicate variability of both energy density and slip. Data from the laboratory studies in which G′ was obtained from the inversion of acoustic emissions are included together with the seismological data.

natural fault scale. Laboratory estimates saturate at high slip values, a feature that is not shown by seismological data. However, the deviations due to saturation lie within the dispersion of data over the entire slip range.

The scaling of fracture energy and breakdown work with slip can be interpreted in terms of both off-fault damage, because W_{off} scales with rupture length and slip, and the continuous degradation of shear stress with slip, due to thermal weakening or pore fluid pressurization. The inferred fracture energy scaling with slip for lab-quakes and microearthquakes might be interpreted in terms of large-scale inelastic yielding (Fialko 2015) because in this case the size of the rupture front zone might correspond to a large fraction of the rupture length. This raises the question of interpreting the constant fracture energy inferred from laboratory experiments dealing with material strength and toughness. A possible interpretation is that these material-dependent constant fracture energies are important at the microscale for fracturing grains composing the gouge or microasperities of sliding surfaces, and indeed they are used to measure the specific surface energy and on-fault dissipation (W_{on}), but they do not govern the dissipation process during the earthquake rupture propagation on a geological fault at the macroscale. Once again this raises the question of the energy dissipated at the microscale by microphysical processes with respect to the macroscopic energy dissipation. The adoption of a macroscopic interpretation means that we focus on the work spent to sustain shear stress evolution and slip on the fault zone. The interpretation of this energy consumption in terms of microscale processes is possible but often model dependent.

A further consideration concerns the normal stress. In most laboratory experiments and modeling attempts, it is assumed that normal stress is constant. Exceptions include the poroelastic response of thick fault zones with variable permeability and porosity. Here we limit our review to recall that, if normal stress changes during coseismic rupture, the work due to slip-induced dilation or compaction must be summed to the work due to shear dislocation to contribute to the total work during slip (Fulton & Rathbun 2011).

In conclusion, different theoretical approaches have been proposed to interpret the dynamic rupture propagation and the involved energy dissipation mechanisms, such as LEFM, rate- and state-dependent friction, or thermal weakening. These approaches are extremely useful and powerful to explain some of the features of a complex, highly nonlinear process as the dynamic weakening and rupture propagation along a geological fault. They are certainly successful to describe and interpret specific configurations of the problem: for example, the adoption of LEFM to model the rupture propagation on a fault zone characterized by linear elastic driving energy at the macroscale of the fault zone and edge-localized dissipation at the shorter scale of the rupture front zone (Brener & Bouchbinder 2021); or similarly, the adoption of thermal weakening (e.g., flash heating) to model the shear stress evolution of a fault zone at high slip velocities (Nielsen et al. 2021, Rice 2006, Viesca & Garagash 2015, among many others). Here, we remark that these theoretical approaches are not exclusive because of the heterogeneities of geological faults and the complexity of the rupture process and loading conditions. In other words, reconciling observations and results from laboratory experiments and numerical modeling with geological observations can be done, provided that we accept the evidence that earthquakes can occur in a variety of geological settings and fault zone structures.

DISCLOSURE STATEMENT

The authors are not aware of any affiliations, memberships, funding, or financial holdings that might be perceived as affecting the objectivity of this review.

ACKNOWLEDGMENTS

The authors thank Production Editor Annie Beck for her continuous support, Illustration Editor Doug Beckner for assistance in figure preparation, and an anonymous reviewer for constructive comments. This review received funding from the European Research Council (ERC) under the European Union's Horizon 2020 research and innovation program. M.C. participated in this work as Principal Investigator of the Horizon 2020 ERC project FEAR (grant 856559). S.A., E.S., E.T., and C.C. participated in this work in the framework of the ERC project FEAR. G.D.T., S.A., C.C., S.B.N., and E.S. acknowledge the ERC CoG 614705 NOFEAR project.

LITERATURE CITED

Aben FM, Brantut N, Mitchell TM. 2020. Off-fault damage characterization during and after experimental quasi-static and dynamic rupture in crustal rock from laboratory *P* wave tomography and microstructures. *J. Geophys. Res. Solid Earth* 125(8):e2020JB019860

Aben FM, Brantut N, Mitchell TM, David EC. 2019. Rupture energetics in crustal rock from laboratory-scale seismic tomography. *Geophys. Res. Lett.* 46(13):7337–44

Abercrombie RE. 2021. Resolution and uncertainties in estimates of earthquake stress drop and energy release. *Philos. Trans. R. Soc. A* 379(2196):20200131

Abercrombie RE, McGarr A, Di Toro G, Kanamori H, eds. 2006. *Earthquakes: Radiated Energy and the Physics of Faulting*. Geophys. Monogr. Ser. Vol. 170. Washington, DC: AGU

Abercrombie RE, Rice JR. 2005. Can observations of earthquake scaling constrain slip weakening? *Geophys. J. Int.* 162(2):406–24

Acosta M, Passelègue FX, Schubnel A, Violay M. 2018. Dynamic weakening during earthquakes controlled by fluid thermodynamics. *Nat. Commun.* 9(1):3074

Aki K. 1980. Attenuation of shear-waves in the lithosphere for frequencies from 0.05 to 25 Hz. *Phys. Earth Planet. Inter.* 21(1):50–60

Andrews DJ. 1976a. Rupture propagation with finite stress in antiplane strain. *J. Geophys. Res.* 81(20):3575–82

Andrews DJ. 1976b. Rupture velocity of plane strain shear cracks. *J. Geophys. Res.* 81(32):5679–87

Andrews DJ. 2005. Rupture dynamics with energy loss outside the slip zone. *J. Geophys. Res.* 110(B1):B01307
Andrews DJ, Ben-Zion Y. 1997. Wrinkle-like slip pulse on a fault between different materials. *J. Geophys. Res.* 102(B1):553–71
Archard JF. 1959. The temperature of rubbing surfaces. *Wear* 2(6):438–55
Aretusini S, Meneghini F, Spagnuolo E, Harbord CW, Di Toro G. 2021a. Fluid pressurisation and earthquake propagation in the Hikurangi subduction zone. *Nat. Commun.* 12(1):2481
Aretusini S, Núñez-Cascajero A, Spagnuolo E, Tapetado A, Vázquez C, Di Toro G. 2021b. Fast and localized temperature measurements during simulated earthquakes in carbonate rocks. *Geophys. Res. Lett.* 48(9):e2020GL091856
Aubry J, Passelègue FX, Deldicque D, Girault F, Marty S, et al. 2018. Frictional heating processes and energy budget during laboratory earthquakes. *Geophys. Res. Lett.* 45(22):12274–82
Austrheim H, Boundy MT. 1994. Pseudotachylytes generated during seismic faulting and eclogitization of the deep crust. *Science* 265(5168):82–83
Barenblatt GI. 1959. The formation of equilibrium cracks during brittle fracture. General ideas and hypotheses. Axially-symmetric cracks. *J. Appl. Math. Mech.* 23(3):622–36
Barras F, Aldam M, Roch T, Brener EA, Bouchbinder E, Molinari JF. 2020. The emergence of crack-like behavior of frictional rupture: edge singularity and energy balance. *Earth Planet. Sci. Lett.* 531:115978
Bayart E, Svetlizky I, Fineberg J. 2016. Fracture mechanics determine the lengths of interface ruptures that mediate frictional motion. *Nat. Phys.* 12(2):166–70
Bayart E, Svetlizky I, Fineberg J. 2018. Rupture dynamics of heterogeneous frictional interfaces. *J. Geophys. Res. Solid Earth* 123(5):3828–48
Beeler NM. 2006. Inferring earthquake source properties from laboratory observations and the scope of lab contributions to source physics. See Abercrombie et al. 2006, pp. 99–119
Beeler NM. 2007. Laboratory-observed faulting in intrinsically and apparently weak materials: strength, seismic coupling, dilatancy, and pore-fluid pressure. In *The Seismogenic Zone of Subduction Thrust Faults*, ed. TH Dixon, C Moore, pp. 370–449. New York: Columbia Univ. Press
Beeler NM, Kilgore B, McGarr A, Fletcher J, Evans J, Baker SR. 2012. Observed source parameters for dynamic rupture with non-uniform initial stress and relatively high fracture energy. *J. Struct. Geol.* 38:77–89
Ben-Zion Y. 2001. On quantification of the earthquake source. *Seismol. Res. Lett.* 72(2):151–52
Ben-Zion Y, Ampuero J-P. 2009. Seismic radiation from regions sustaining material damage. *Geophys. J. Int.* 178(3):1351–56
Ben-Zion Y, Sammis CG. 2013. Shear heating during distributed fracturing and pulverization of rocks. *Geology* 41(2):139–42
Biegel RL, Sammis CG, Rosakis AJ. 2008. An experimental study of the effect of off-fault damage on the velocity of a slip pulse. *J. Geophys. Res.* 113(B4):B04302
Billi A, Storti F. 2004. Fractal distribution of particle size in carbonate cataclastic rocks from the core of a regional strike-slip fault zone. *Tectonophysics* 384(1):115–28
Bizzarri A. 2010. On the relations between fracture energy and physical observables in dynamic earthquake models. *J. Geophys. Res.* 115(B10):B10307
Bizzarri A. 2011. On the deterministic description of earthquakes. *Rev. Geophys.* 49(3):RG3002
Bizzarri A, Cocco M. 2006. A thermal pressurization model for the spontaneous dynamic rupture propagation on a three-dimensional fault: 1. Methodological approach. *J. Geophys. Res.* 111(B5):B05303
Bouchon M. 1997. The state of stress on some faults of the San Andreas system as inferred from near-field strong motion data. *J. Geophys. Res.* 102(B6):11731–44
Boulton C, Yao L, Faulkner DR, Townend J, Toy VG, et al. 2017. High-velocity frictional properties of Alpine Fault rocks: mechanical data, microstructural analysis, and implications for rupture propagation. *J. Struct. Geol.* 97:71–92
Boutareaud S, Hirose T, Andréani M, Pec M, Calugaru D-G, et al. 2012. On the role of phyllosilicates on fault lubrication: insight from micro- and nanostructural investigations on talc friction experiments. *J. Geophys. Res.* 117(B8):B08408
Brace WF, Walsh JB. 1962. Some direct measurements of the surface energy of quartz and orthoclase. *Am. Mineral.* 47(9–10):1111–22

Brantut N, Heap MJ, Meredith PG, Baud P. 2013. Time-dependent cracking and brittle creep in crustal rocks: a review. *J. Struct. Geol.* 52:17–43

Brantut N, Schubnel A, Rouzaud J-N, Brunet F, Shimamoto T. 2008. High-velocity frictional properties of a clay-bearing fault gouge and implications for earthquake mechanics. *J. Geophys. Res.* 113(B10):B10401

Brantut N, Viesca RC. 2017. The fracture energy of ruptures driven by flash heating. *Geophys. Res. Lett.* 44(13):6718–25

Brener EA, Bouchbinder E. 2021. Unconventional singularities and energy balance in frictional rupture. *Nat. Commun.* 12(1):2585

Broberg KB. 1978. On transient sliding motion. *Geophys. J. Int.* 52(3):397–432

Brodsky EE, Kanamori H. 2001. Elastohydrodynamic lubrication of faults. *J. Geophys. Res.* 106(B8):16357–74

Brodsky EE, Mori JJ, Anderson L, Chester FM, Conin M, et al. 2020. The state of stress on the fault before, during, and after a major earthquake. *Annu. Rev. Earth Planet. Sci.* 48:49–74

Brune JN. 1970. Tectonic stress and the spectra of seismic shear waves from earthquakes. *J. Geophys. Res.* 75(26):4997–5009

Caine JS, Evans JP, Forster CB. 1996. Fault zone architecture and permeability structure. *Geology* 24(11):1025–28

Causse M, Dalguer LA, Mai PM. 2014. Variability of dynamic source parameters inferred from kinematic models of past earthquakes. *Geophys. J. Int.* 196(3):1754–69

Chang JC, Lockner AD, Reches Z. 2012. Rapid acceleration leads to rapid weakening in earthquake-like laboratory experiments. *Science* 338(6103):101–5

Chen J, Niemeijer AR, Fokker PA. 2017. Vaporization of fault water during seismic slip. *J. Geophys. Res. Solid Earth* 122(6):4237–76

Chen X, Chitta SS, Zu X, Reches Z. 2021. Dynamic fault weakening during earthquakes: rupture or friction? *Earth Planet. Sci. Lett.* 575:117165

Chester FM, Chester JS. 1998. Ultracataclasite structure and friction processes of the Punchbowl fault, San Andreas system, California. *Tectonophysics* 295(1–2):199–221

Chester FM, Chester JS, Kirschner DL, Schulz SE, Evans JP. 2004. Structure of large-displacement, strike-slip fault zones in the brittle continental crust. In *Rheology and Deformation of the Lithosphere at Continental Margins*, ed. GD Karner, B Taylor, NW Driscoll, DL Kohlstedt, pp. 223–60. New York: Columbia Univ. Press

Chester FM, Evans JP, Biegel RL. 1993. Internal structure and weakening mechanisms of the San Andreas Fault. *J. Geophys. Res.* 98(B1):771–86

Chester FM, Logan JM. 1986. Implications for mechanical properties of brittle faults from observations of the Punchbowl fault zone, California. *Pure Appl. Geophys.* 124(1):79–106

Chester JS, Chester FM, Kronenberg AK. 2005. Fracture surface energy of the Punchbowl fault, San Andreas system. *Nature* 437(7055):133–36

Choi J-H, Edwards P, Ko K, Kim Y-S. 2016. Definition and classification of fault damage zones: a review and a new methodological approach. *Earth-Sci. Rev.* 152:70–87

Cocco M, Bizzarri A. 2002. On the slip-weakening behavior of rate- and state dependent constitutive laws. *Geophys. Res. Lett.* 29(11):1516

Cocco M, Spudich P, Tinti E. 2006. On the mechanical work absorbed on faults during earthquake ruptures. See Abercrombie et al. 2006, pp. 237–54

Cocco M, Tinti E. 2008. Scale dependence in the dynamics of earthquake propagation: evidence from seismological and geological observations. *Earth Planet. Sci. Lett.* 273(1–2):123–31

Cocco M, Tinti E, Cirella A. 2016. On the scale dependence of earthquake stress drop. *J. Seismol.* 20(4):1151–70

Collettini C, Viti C, Tesei T, Mollo S. 2013. Thermal decomposition along natural carbonate faults during earthquakes. *Geology* 41(8):927–30

Cornelio C, Passelègue FX, Spagnuolo E, Di Toro G, Violay M. 2020. Effect of fluid viscosity on fault reactivation and coseismic weakening. *J. Geophys. Res. Solid Earth* 125:e2019JB018883

Cornelio C, Spagnuolo E, Aretusini S, Nielsen S, Passelègue F, et al. 2022. Determination of parameters characteristic of dynamic weakening mechanisms during seismic faulting in cohesive rocks. *J. Geophys. Res. Solid Earth* 127:e2022JB024356

Cornelio C, Spagnuolo E, Di Toro G, Nielsen SB, Violay M. 2019. Mechanical behaviour of fluid-lubricated faults. *Nat. Commun.* 10(1):1274

Cowie PA, Attal M, Tucker GE, Whittaker AC, Naylor M, et al. 2006. Investigating the surface process response to fault interaction and linkage using a numerical modelling approach. *Basin Res.* 18(3):231–66

De Paola N, Hirose T, Mitchell T, Di Toro G, Viti C, Shimamoto T. 2011. Fault lubrication and earthquake propagation in thermally unstable rocks. *Geology* 39(1):35–38

De Paola N, Holdsworth RE, Viti C, Collettini C, Bullock R. 2015. Can grain size sensitive flow lubricate faults during the initial stages of earthquake propagation? *Earth Planet. Sci. Lett.* 431:48–58

Del Gaudio P, Di Toro G, Han R, Hirose T, Nielsen SB, et al. 2009. Frictional melting of peridotite and seismic slip. *J. Geophys. Res.* 114(B6):B06306

Delle Piane C, Clennell MB, Keller JVA, Giwelli A, Luzin V. 2017. Carbonate hosted fault rocks: a review of structural and microstructural characteristic with implications for seismicity in the upper crust. *J. Struct. Geol.* 103:17–36

Demurtas M, Fondriest M, Balsamo F, Clemenzi L, Storti F, et al. 2016. Structure of a normal seismogenic fault zone in carbonates: the Vado di Corno Fault, Campo Imperatore, Central Apennines (Italy). *J. Struct. Geol.* 90:185–206

Demurtas M, Smith SAF, Prior DJ, Brenker FE, Di Toro G. 2019. Grain size sensitive creep during simulated seismic slip in nanogranular fault gouges: constraints from transmission Kikuchi diffraction (TKD). *J. Geophys. Res. Solid Earth* 124(10):10197–209

Di Toro G, Aretusini S, Cornelio C, Nielsen S, Spagnuolo E, et al. 2021. Friction during earthquakes: 25 years of experimental studies. *IOP Conf. Ser. Earth Environ. Sci.* 861:052032

Di Toro G, Han R, Hirose T, De Paola N, Nielsen S, et al. 2011. Fault lubrication during earthquakes. *Nature* 471(7339):494–98

Di Toro G, Hirose T, Nielsen SB, Pennacchioni G, Shimamoto T. 2006. Natural and experimental evidence of melt lubrication of faults during earthquakes. *Science* 311(5761):647–49

Di Toro G, Nielsen S, Pennacchioni G. 2005a. Earthquake rupture dynamics frozen in exhumed ancient faults. *Nature* 436(7053):1009–12

Di Toro G, Pennacchioni G, Teza G. 2005b. Can pseudotachylytes be used to infer earthquake source parameters? An example of limitations in the study of exhumed faults. *Tectonophysics* 402(1–4):3–20

Dieterich JH. 1979. Modeling of rock friction: 1. Experimental results and constitutive equations. *J. Geophys. Res.* 84(B5):2161–68

Dor O, Ben-Zion Y, Rockwell TK, Brune J. 2006. Pulverized rocks in the Mojave section of the San Andreas Fault Zone. *Earth Planet. Sci. Lett.* 245(3):642–54

Dunham EM, Belanger D, Cong L, Kozdon JE. 2011a. Earthquake ruptures with strongly rate-weakening friction and off-fault plasticity, Part 1: Planar faults. *Bull. Seismol. Soc. Am.* 101(5):2296–307

Dunham EM, Belanger D, Cong L, Kozdon JE. 2011b. Earthquake ruptures with strongly rate-weakening friction and off-fault plasticity, Part 2: Nonplanar faults. *Bull. Seismol. Soc. Am.* 101(5):2308–22

Faulkner DR, Jackson CAL, Lunn RJ, Schlische RW, Shipton ZK, et al. 2010. A review of recent developments concerning the structure, mechanics and fluid flow properties of fault zones. *J. Struct. Geol.* 32(11):1557–75

Faulkner DR, Lewis AC, Rutter EH. 2003. On the internal structure and mechanics of large strike-slip fault zones: field observations of the Carboneras fault in southeastern Spain. *Tectonophysics* 367(3):235–51

Faulkner DR, Mitchell TM, Behnsen J, Hirose T, Shimamoto T. 2011. Stuck in the mud? Earthquake nucleation and propagation through accretionary forearcs. *Geophys. Res. Lett.* 38(18):L18303

Favreau P, Archuleta RJ. 2003. Direct seismic energy modeling and application to the 1979 Imperial Valley earthquake. *Geophys. Res. Lett.* 30(5):1198

Fialko Y. 2015. Fracture and frictional mechanics: theory. In *Treatise on Geophysics*, Vol. 4, ed. G Schubert, pp. 73–91. Amsterdam: Elsevier. 2nd ed.

Fondriest M, Aretusini S, Di Toro G, Smith SAF. 2015. Fracturing and rock pulverization along an exhumed seismogenic fault zone in dolostones: the Foiana Fault Zone (Southern Alps, Italy). *Tectonophysics* 654:56–74

Fondriest M, Balsamo F, Bistacchi A, Clemenzi L, Demurtas M, et al. 2020. Structural complexity and mechanics of a shallow crustal seismogenic source (Vado di Corno Fault Zone, Italy). *J. Geophys. Res. Solid Earth* 125(9):e2019JB018926

Fondriest M, Smith SAF, Candela T, Nielsen SB, Mair K, Di Toro G. 2013. Mirror-like faults and power dissipation during earthquakes. *Geology* 41(11):1175–78

French ME, Kitajima H, Chester JS, Chester FM, Hirose T. 2014. Displacement and dynamic weakening processes in smectite-rich gouge from the Central Deforming Zone of the San Andreas Fault. *J. Geophys. Res. Solid Earth* 119(3):1777–802

Freund LB. 1979. The mechanics of dynamic shear crack propagation. *J. Geophys. Res.* 84(B5):2199–209

Fukuyama E, Madariaga R. 1998. Rupture dynamics of a planar fault in a 3D elastic medium: rate- and slip-weakening friction. *Bull. Seismol. Soc. Am.* 88(1):1–17

Fulton PM, Rathbun AP. 2011. Experimental constraints on energy partitioning during stick-slip and stable sliding within analog fault gouge. *Earth Planet. Sci. Lett.* 308(1):185–92

Gallovič F, Valentová L', Ampuero J-P, Gabriel A-A. 2019. Bayesian dynamic finite-fault inversion: 1. Method and synthetic test. *J. Geophys. Res. Solid Earth* 124(7):6949–69

Gallovič F, Zahradník J, Plicka V, Sokos E, Evangelidis C, et al. 2020. Complex rupture dynamics on an immature fault during the 2020 Mw 6.8 Elazığ earthquake, Turkey. *Commun. Earth Environ.* 1(1):40

Giacomel P, Spagnuolo E, Nazzari M, Marzoli A, Passelegue F, et al. 2018. Frictional instabilities and carbonation of basalts triggered by injection of pressurized H_2O- and CO_2-rich fluids. *Geophys. Res. Lett.* 45(12):6032–41

Goldsby DL, Tullis TE. 2011. Flash heating leads to low frictional strength of crustal rocks at earthquake slip rates. *Science* 334(6053):216–18

Green HW II, Shi F, Bozhilov K, Xia G, Reches Z. 2015. Phase transformation and nanometric flow cause extreme weakening during fault slip. *Nat. Geosci.* 8(6):484–89

Gregg JM. 1983. On the formation and occurrence of saddle dolomite: discussion. *J. Sediment. Res.* 53(3):1025–26

Griffith AA. 1921. VI. The phenomena of rupture and flow in solids. *Philos. Trans. R. Soc. A* 221(582–93):163–98

Griffith WA, Nielsen SB, Di Toro G, Smith SAF. 2010. Rough faults, distributed weakening, and off-fault deformation. *J. Geophys. Res.* 115(8):B08409

Guatteri M, Mai PM, Beroza GC, Boatwright J. 2003. Strong ground-motion prediction from stochastic-dynamic source models. *Bull. Seismol. Soc. Am.* 93(1):301–13

Guatteri M, Spudich P. 2000. What can strong-motion data tell us about slip-weakening fault-friction laws? *Bull. Seismol. Soc. Am.* 90(1):98–116

Guatteri M, Spudich P, Beroza GC. 2001. Inferring rate and state friction parameters from a rupture model of the 1995 Hyogo-ken Nanbu (Kobe) Japan earthquake. *J. Geophys. Res.* 106(B11):26511–21

Guérin-Marthe S, Nielsen SB, Bird R, Giani S, Di Toro G. 2019. Earthquake nucleation size: evidence of loading rate dependence in laboratory faults. *J. Geophys. Res. Solid Earth* 124(1):689–708

Hakami H, Stephansson O. 1990. Shear fracture energy of Stripa granite—results of controlled triaxial testing. *Eng. Fract. Mech.* 35(4):855–65

Han R, Hirose T, Shimamoto T. 2010. Strong velocity weakening and powder lubrication of simulated carbonate faults at seismic slip rates. *J. Geophys. Res.* 115(B3):B03412

Han R, Shimamoto T, Hirose T, Ree J-H, Ando J. 2007. Ultralow friction of carbonate faults caused by thermal decomposition. *Science* 316(5826):878–81

Harbord C, Brantut N, Spagnuolo E, Di Toro G. 2021. Fault friction during simulated seismic slip pulses. *J. Geophys. Res. Solid Earth* 126(8):e2021JB022149

Harris RA. 2017. Large earthquakes and creeping faults. *Rev. Geophys.* 55(1):169–98

Heaton TH. 1990. Evidence for and implications of self-healing pulses of slip in earthquake rupture. *Phys. Earth Planet. Inter.* 64(1):1–20

Hirose T, Bystricky M. 2007. Extreme dynamic weakening of faults during dehydration by coseismic shear heating. *Geophys. Res. Lett.* 34(14):L14311

Hou L, Ma S, Shimamoto T, Chen J, Yao L, et al. 2012. Internal structures and high-velocity frictional properties of a bedding-parallel carbonate fault at Xiaojiaqiao outcrop activated by the 2008 Wenchuan earthquake. *Earthq. Sci.* 25(3):197–217

Ida Y. 1972. Cohesive force across the tip of a longitudinal-shear crack and Griffith's specific surface energy. *J. Geophys. Res.* 77(20):3796–805

Ide S, Takeo M. 1997. Determination of constitutive relations of fault slip based on seismic wave analysis. *J. Geophys. Res.* 102(B12):27379–91

Ikari MJ, Ito Y, Ujiie K, Kopf AJ. 2015. Spectrum of slip behaviour in Tohoku fault zone samples at plate tectonic slip rates. *Nat. Geosci.* 8(11):870–74

Irwin GR. 1956. *Onset of fast crack propagation in high strength steel and aluminum alloys*. NRL Rep. 4763, Nav. Res. Lab., Washington DC

Irwin GR. 1957. Analysis of stresses and strains near the end of a crack traversing a plate. *J. Appl. Mech.* 24(3):361–64

Johnson SE, Song WJ, Vel SS, Song BR, Gerbi CC. 2021. Energy partitioning, dynamic fragmentation, and off-fault damage in the earthquake source volume. *J. Geophys. Res. Solid Earth* 126(11):e2021JB022616

Kammer DS, McLaskey GC. 2019. Fracture energy estimates from large-scale laboratory earthquakes. *Earth Planet. Sci. Lett.* 511:36–43

Kanamori H, Rivera L. 2006. Energy partitioning during an earthquake. See Abercrombie et al. 2006, pp. 3–13

Ke C-Y, McLaskey GC, Kammer DS. 2018. Rupture termination in laboratory-generated earthquakes. *Geophys. Res. Lett.* 45(23):12784–92

Knopoff L. 1958. Energy release in earthquakes. *Geophys. J. Int.* 1(1):44–52

Kostrov BV, Das S. 1988. *Principles of Earthquake Source Mechanics*. Cambridge, UK: Cambridge Univ. Press

Lachenbruch AH, Sass JH. 1980. Heat flow and energetics of the San Andreas fault zone. *J. Geophys. Res.* 85(10):6185–222

Lambert V, Lapusta N. 2020. Rupture-dependent breakdown energy in fault models with thermo-hydro-mechanical processes. *Solid Earth* 11(6):2283–302

Liu Z, Rummel F. 1990. Shear fracture energy of rock at high pressure and high temperature. *Phys. Chem. Earth* 17:99–109

Lockner DA, Byerlee JD, Kuksenko V, Ponomarev A, Sidorin A. 1991. Quasi-static fault growth and shear fracture energy in granite. *Nature* 350(6313):39–42

Lockner DA, Okubo PG. 1983. Measurements of frictional heating in granite. *J. Geophys. Res.* 88(B5):4313–20

Lyakhovsky V. 2001. Scaling of fracture length and distributed damage. *Geophys. J. Int.* 144:114–22

Ma K-F, Tanaka H, Song S-R, Wang C-Y, Hung J-H, et al. 2006. Slip zone and energetics of a large earthquake from the Taiwan Chelungpu-fault Drilling Project. *Nature* 444(7118):473–76

Madariaga R. 1978. The dynamic field of Haskell's rectangular dislocation fault model. *Bull. Seismol. Soc. Am.* 68(4):869–87

Mai PM, Somerville P, Pitarka A, Dalguer L, Song S, et al. 2006. On scaling of fracture energy and stress drop in dynamic rupture models: consequences for near-source ground-motions. See Abercrombie et al. 2006, pp. 283–93

Mai PM, Thingbaijam KKS. 2014. SRCMOD: an online database of finite-fault rupture models. *Seismol. Res. Lett.* 85(6):1348–57

Malagnini L, Munafo' I, Cocco M, Nielsen S, Mayeda K, Boschi E. 2014. Gradual fault weakening with seismic slip: inferences from the seismic sequences of L'Aquila, 2009, and Northridge, 1994. *Pure Appl. Geophys.* 171(10):2709–30

Marone C. 1998. Laboratory-derived friction laws and their application to seismic faulting. *Annu. Rev. Earth Planet. Sci.* 26:643–96

Masoch S, Gomila R, Fondriest M, Jensen E, Mitchell T, et al. 2021. Structural evolution of a crustal-scale seismogenic fault in a magmatic arc: the Bolfin Fault Zone (Atacama Fault System). *Tectonics* 40(8):e2021TC006818

McLaskey GC, Kilgore BD, Beeler NM. 2015. Slip-pulse rupture behavior on a 2 m granite fault. *Geophys. Res. Lett.* 42(17):7039–45

McLaskey GC, Kilgore BD, Lockner DA, Beeler NM. 2014. Laboratory generated M-6 earthquakes. *Pure Appl. Geophys.* 171(10):2601–15

Mia MS, Abdelmeguid M, Elbanna AE. 2022. Spatio-temporal clustering of seismicity enabled by off-fault plasticity. *Geophys. Res. Lett.* 49(8):e2021GL097601

Mitchell TM, Faulkner DR. 2009. The nature and origin of off-fault damage surrounding strike-slip fault zones with a wide range of displacements: a field study from the Atacama fault system, northern Chile. *J. Struct. Geol.* 31(8):802–16

Mizoguchi K, Hirose T, Shimamoto T, Fukuyama E. 2007. Reconstruction of seismic faulting by high-velocity friction experiments: an example of the 1995 Kobe earthquake. *Geophys. Res. Lett.* 34(1):L01308

Moore DE, Lockner DA. 1995. The role of microcracking in shear-fracture propagation in granite. *J. Struct. Geol.* 17(1):95–114

Murphy S, Di Toro G, Romano F, Scala A, Lorito S, et al. 2018. Tsunamigenic earthquake simulations using experimentally derived friction laws. *Earth Planet. Sci. Lett.* 486:155–65

Nielsen S, Di Toro G, Hirose T, Shimamoto T. 2008. Frictional melt and seismic slip. *J. Geophys. Res.* 113(B1):B01308

Nielsen S, Madariaga R. 2003. On the self-healing fracture mode. *Bull. Seismol. Soc. Am.* 93(6):2375–88

Nielsen S, Spagnuolo E, Smith SAF, Violay M, Di Toro G, Bistacchi A. 2016a. Scaling in natural and laboratory earthquakes. *Geophys. Res. Lett.* 43(4):1504–10

Nielsen S, Spagnuolo E, Violay M, Di Toro G. 2021. Thermal weakening friction during seismic slip: experiments and models with heat sources and sinks. *J. Geophys. Res. Solid Earth* 126(5):e2020JB020652

Nielsen S, Spagnuolo E, Violay M, Smith S, Di Toro G, Bistacchi A. 2016b. G: fracture energy, friction and dissipation in earthquakes. *J. Seismol.* 20(4):1187–205

Niemeijer A, Di Toro G, Griffith WA, Bistacchi A, Smith SAF, Nielsen S. 2012. Inferring earthquake physics and chemistry using an integrated field and laboratory approach. *J. Struct. Geol.* 39:2–36

Ohl M, Plümper O, Chatzaras V, Wallis D, Vollmer C, Drury M. 2020. Mechanisms of fault mirror formation and fault healing in carbonate rocks. *Earth Planet. Sci. Lett.* 530:115886

Ohnaka M. 1996. Nonuniformity of the constitutive law parameters for shear rupture and quasistatic nucleation to dynamic rupture: a physical model of earthquake generation processes. *PNAS* 93(9):3795–802

Ohnaka M. 2003. A constitutive scaling law and a unified comprehension for frictional slip failure, shear fracture of intact rock, and earthquake rupture. *J. Geophys. Res.* 108(B2):2080

Ohnaka M. 2013. *The Physics of Rock Failure and Earthquakes*. Cambridge, UK: Cambridge Univ. Press

Ohnaka M, Akatsu M, Mochizuki H, Odedra A, Tagashira F, Yamamoto Y. 1997. A constitutive law for the shear failure of rock under lithospheric conditions. *Tectonophysics* 277(1):1–27

Ohnaka M, Shen L. 1999. Scaling of the shear rupture process from nucleation to dynamic propagation: implications of geometric irregularity of the rupturing surfaces. *J. Geophys. Res.* 104(B1):817–44

Ohnaka M, Yamashita T. 1989. A cohesive zone model for dynamic shear faulting based on experimentally inferred constitutive relation and strong motion source parameters. *J. Geophys. Res.* 94(B4):4089–104

Okubo K, Bhat HS, Rougier E, Marty S, Schubnel A, et al. 2019. Dynamics, radiation, and overall energy budget of earthquake rupture with coseismic off-fault damage. *J. Geophys. Res. Solid Earth* 124(11):11771–801

Okubo PG, Dieterich JH. 1981. Fracture energy of stick-slip events in a large scale biaxial experiment. *Geophys. Res. Lett.* 8(8):887–90

Okubo PG, Dieterich JH. 1984. Effects of physical fault properties on frictional instabilities produced on simulated faults. *J. Geophys. Res.* 89(B7):5817–27

Oohashi K, Hirose T, Takahashi M, Tanikawa W. 2015. Dynamic weakening of smectite-bearing faults at intermediate velocities: implications for subduction zone earthquakes. *J. Geophys. Res. Solid Earth* 120(3):1572–86

Ostermeijer GA, Mitchell TM, Aben FM, Dorsey MT, Browning J, et al. 2020. Damage zone heterogeneity on seismogenic faults in crystalline rock; a field study of the Borrego Fault, Baja California. *J. Struct. Geol.* 137:104016

Paglialunga F, Passelègue FX, Brantut N, Barras F, Lebihain M, Violay M. 2022. On the scale dependence in the dynamics of frictional rupture: constant fracture energy versus size-dependent breakdown work. *Earth Planet. Sci. Lett.* 584:117442

Palmer AC, Rice JR. 1973. The growth of slip surfaces in the progressive failure of over-consolidated clay. *Proc. R. Soc. A.* 332(1591):527–48

Passelègue FX, Latour S, Schubnel A, Nielsen S, Bhat HS, Madariaga R. 2017. Influence of fault strength on precursory processes during laboratory earthquakes. In *Fault Zone Dynamic Processes: Evolution of*

Fault Properties During Seismic Rupture, ed. MY Thomas, TM Mitchell, HS Bhat, pp. 229–42. Geophys. Monogr. Ser. Vol. 227. Washington, DC: AGU

Passelègue FX, Schubnel A, Nielsen SB, Bhat HS, Deldicque D, Madariaga R. 2016a. Dynamic rupture processes inferred from laboratory microearthquakes. *J. Geophys. Res. Solid Earth* 121(6):4343–65

Passelègue FX, Spagnuolo E, Violay M, Nielsen SB, Di Toro G, Schubnel A. 2016b. Frictional evolution, acoustic emissions activity, and off-fault damage in simulated faults sheared at seismic slip rates. *J. Geophys. Res. Solid Earth* 121(10):7490–513

Paterson MS, Wong T. 2005. *Experimental Rock Deformation—The Brittle Field*. Berlin: Springer-Verlag

Pec M, Stünitz H, Heilbronner R, Drury M, de Capitani C. 2012. Origin of pseudotachylites in slow creep experiments. *Earth Planet. Sci. Lett.* 355–56:299–310

Peng Z, Gomberg J. 2010. An integrated perspective of the continuum between earthquakes and slow-slip phenomena. *Nat. Geosci.* 3(9):599–607

Peyrat S, Olsen K, Madariaga R. 2001. Dynamic modeling of the 1992 Landers earthquake. *J. Geophys. Res.* 106(B11):26467–82

Pittarello L, Di Toro G, Bizzarri A, Pennacchioni G, Hadizadeh J, Cocco M. 2008. Energy partitioning during seismic slip in pseudotachylyte-bearing faults (Gole Larghe Fault, Adamello, Italy). *Earth Planet. Sci. Lett.* 269(1):131–39

Pozzi G, De Paola N, Holdsworth RE, Bowen L, Nielsen SB, Dempsey ED. 2019. Coseismic ultramylonites: an investigation of nanoscale viscous flow and fault weakening during seismic slip. *Earth Planet. Sci. Lett.* 516:164–75

Pozzi G, De Paola N, Nielsen SB, Holdsworth RE, Bowen L. 2018. A new interpretation for the nature and significance of mirror-like surfaces in experimental carbonate-hosted seismic faults. *Geology* 46(7):583–86

Rabinowicz E. 1966. Friction and wear of materials. *J. Appl. Mech.* 33(2):479

Reches Z, Dewers TA. 2005. Gouge formation by dynamic pulverization during earthquake rupture. *Earth Planet. Sci. Lett.* 235(1):361–74

Reid HF. 1910. *The California Earthquake of April 18, 1906*, Vol. 2: *The Mechanics of the Earthquake*. Washington, DC: Carnegie Inst.

Rempe M, Smith S, Mitchell T, Hirose T, Di Toro G. 2017. The effect of water on strain localization in calcite fault gouge sheared at seismic slip rates. *J. Struct. Geol.* 97:104–17

Rice JR. 1968. A path independent integral and the approximate analysis of strain concentration by notches and cracks. *J. Appl. Mech.* 35:379–86

Rice JR. 1979. The mechanics of earthquake rupture. In *Physics of Earth's Interior*, ed. AM Dziewonski, E Boschi, pp. 555–649. New York: North-Holland

Rice JR. 2006. Heating and weakening of faults during earthquake slip. *J. Geophys. Res.* 111(B5):B05311

Rice JR, Cocco M. 2007. Seismic fault rheology and earthquake dynamics. *The Dynamics of Fault Zones*, ed. MR Handy, pp. 16–21. Cambridge, MA: MIT Press

Rice JR, Sammis CG, Parsons R. 2005. Off-fault secondary failure induced by a dynamic slip pulse. *Bull. Seismol. Soc. Am.* 95(1):109–34

Rivera L, Kanamori H. 2005. Representations of the radiated energy in earthquakes. *Geophys. J. Int.* 162(1):148–55

Rockwell T, Sisk M, Girty G, Dor O, Wechsler N, Ben-Zion Y. 2009. Chemical and physical characteristics of pulverized Tejon Lookout Granite adjacent to the San Andreas and Garlock faults: implications for earthquake physics. *Pure Appl. Geophys.* 166(10):1725–46

Rosakis AJ. 2002. Intersonic shear cracks and fault ruptures. *Adv. Phys.* 51(4):1189–257

Rowe CD, Moore JC, Meneghini F, McKeirnan AW. 2005. Large-scale pseudotachylytes and fluidized cataclasites from an ancient subduction thrust fault. *Geology* 33(12):937–40

Ruina A. 1983. Slip instability and state variable friction laws. *J. Geophys. Res.* 88(B12):10359–70

Rummel F, Alheid HJ, Frohn C. 1978. Dilatancy and fracture induced velocity changes in rock and their relation to frictional sliding. *Pure Appl. Geophys.* 116(4):743–64

Sammis C, King G, Biegel R. 1987. The kinematics of gouge deformation. *Pure Appl. Geophys.* 125(5):777–812

Sammis CG, King GCP. 2007. Mechanical origin of power law scaling in fault zone rock. *Geophys. Res. Lett.* 34(4):L04312

Savage HM, Brodsky EE. 2011. Collateral damage: evolution with displacement of fracture distribution and secondary fault strands in fault damage zones. *J. Geophys. Res.* 116(B3):B03405
Sawai M, Hirose T, Kameda J. 2014. Frictional properties of incoming pelagic sediments at the Japan Trench: implications for large slip at a shallow plate boundary during the 2011 Tohoku earthquake. *Earth Planets Space* 66(1):65
Sawai M, Shimamoto T, Togo T. 2012. Reduction in BET surface area of Nojima fault gouge with seismic slip and its implication for the fracture energy of earthquakes. *J. Struct. Geol.* 38:117–38
Scholz CH. 2019. *The Mechanics of Earthquakes and Faulting*. Cambridge, UK: Cambridge Univ. Press. 3rd ed.
Scholz CH, Dawers NH, Yu J-Z, Anders MH, Cowie PA. 1993. Fault growth and fault scaling laws: preliminary results. *J. Geophys. Res.* 98(B12):21951–61
Scuderi MM, Tinti E, Cocco M, Collettini C. 2020. The role of shear fabric in controlling breakdown processes during laboratory slow-slip events. *J. Geophys. Res. Solid Earth* 125(11):e2020JB020405
Sellers EJ, Kataka MO, Linzer LM. 2003. Source parameters of acoustic emission events and scaling with mining-induced seismicity. *J. Geophys. Res.* 108(B9):2418
Selvadurai PA. 2019. Laboratory insight into seismic estimates of energy partitioning during dynamic rupture: an observable scaling breakdown. *J. Geophys. Res. Solid Earth* 124(11):11350–79
Selvadurai PA, Glaser SD. 2017. Asperity generation and its relationship to seismicity on a planar fault: a laboratory simulation. *Geophys. J. Int.* 208(2):1009–25
Seyler CE, Kirkpatrick JD, Savage HM, Hirose T, Faulkner DR. 2020. Rupture to the trench? Frictional properties and fracture energy of incoming sediments at the Cascadia subduction zone. *Earth Planet. Sci. Lett.* 546:116413
Shipton ZK, Soden AM, Kirkpatrick JD, Bright AM, Lunn RJ. 2006. How thick is a fault? Fault displacement-thickness scaling revisited. See Abercrombie et al. 2006, pp. 193–98
Sibson RH. 1975. Generation of pseudotachylyte by ancient seismic faulting. *Geophys. J. R. Astron. Soc.* 43(3):775–94
Sibson RH. 1986. Brecciation processes in fault zones: inferences from earthquake rupturing. *Pure Appl. Geophys.* 124(1–2):159–75
Sibson RH. 2003. Thickness of the seismic slip zone. *Bull. Seismol. Soc. Am.* 93(3):1169–78
Siman-Tov S, Aharonov E, Sagy A, Emmanuel S. 2013. Nanograins form carbonate fault mirrors. *Geology* 41(6):703–6
Smith SAF, Di Toro G, Kim S, Ree J-H, Nielsen S, et al. 2013. Coseismic recrystallization during shallow earthquake slip. *Geology* 41(1):63–66
Spagnuolo E, Plümper O, Violay M, Cavallo A, Di Toro G. 2015. Fast-moving dislocations trigger flash weakening in carbonate-bearing faults during earthquakes. *Sci. Rep.* 5(1):16112
Storti F, Billi A, Salvini F. 2003. Particle size distributions in natural carbonate fault rocks: insights for non-self-similar cataclasis. *Earth Planet. Sci. Lett.* 206(1):173–86
Svetlizky I, Fineberg J. 2014. Classical shear cracks drive the onset of dry frictional motion. *Nature* 509(7499):205–8
Swanson MT. 1988. Pseudotachylyte-bearing strike-slip duplex structures in the Fort Foster Brittle Zone, S. Maine. *J. Struct. Geol.* 10(8):813–28
Tal Y, Faulkner D. 2022. The effect of fault roughness and earthquake ruptures on the evolution and scaling of fault damage zones. *J. Geophys. Res. Solid Earth* 127:e2021JB023352
Tinti E, Casarotti E, Ulrich T, Taufiqurrahman T, Li D, Gabriel A-A. 2021. Constraining families of dynamic models using geological, geodetic and strong ground motion data: the Mw 6.5, October 30th, 2016, Norcia earthquake, Italy. *Earth Planet. Sci. Lett.* 576:117237
Tinti E, Cocco M, Fukuyama E, Piatanesi A. 2009. Dependence of slip weakening distance (D_c) on final slip during dynamic rupture of earthquakes. *Geophys. J. Int.* 177(3):1205–20
Tinti E, Fukuyama E, Piatanesi A, Cocco M. 2005a. A kinematic source-time function compatible with earthquake dynamics. *Bull. Seismol. Soc. Am.* 95(4):1211–23
Tinti E, Spudich P, Cocco M. 2005b. Earthquake fracture energy inferred from kinematic rupture models on extended faults. *J. Geophys. Res.* 110(12):B12303. Erratum. 2008. *J. Geophys. Res.* 113(B7):B07301
Togo T, Shimamoto T. 2012. Energy partition for grain crushing in quartz gouge during subseismic to seismic fault motion: an experimental study. *J. Struct. Geol.* 38:139–55

Togo T, Shimamoto T, Ma S, Hirose T. 2011. High-velocity frictional behavior of Longmenshan fault gouge from Hongkou outcrop and its implications for dynamic weakening of fault during the 2008 Wenchuan earthquake. *Earthq. Sci.* 24(3):267–81

Togo T, Yao L, Ma S, Shimamoto T. 2016. High-velocity frictional strength of Longmenshan fault gouge and its comparison with an estimate of friction from the temperature anomaly in WFSD-1 drill hole. *J. Geophys. Res. Solid Earth* 121(7):5328–48

Tullis TE. 2015. Mechanisms for friction of rock at earthquake slip rates. In *Treatise on Geophysics*, Vol. 4, ed. G Schubert, pp. 131–52. Amsterdam: Elsevier. 2nd ed.

Udias A, Madariaga R, Buforn E. 2014. *Source Mechanisms of Earthquakes*. Cambridge, UK: Cambridge Univ. Press

Ueda T, Obata M, Di Toro G, Kanagawa K, Ozawa K. 2008. Mantle earthquakes frozen in mylonitized ultramafic pseudotachylytes of spinel-lherzolite facies. *Geology* 36(8):607–10

Ujiie K, Tanaka H, Saito T, Tsutsumi A, Mori JJ, et al. 2013. Low coseismic shear stress on the Tohoku-Oki megathrust determined from laboratory experiments. *Science* 342:1211–14

Ujiie K, Tsutsumi A. 2010. High-velocity frictional properties of clay-rich fault gouge in a megasplay fault zone, Nankai subduction zone. *Geophys. Res. Lett.* 37(24):L24310

Ulrich T, Vater S, Madden EH, Behrens J, van Dinther Y, et al. 2019. Coupled, physics-based modeling reveals earthquake displacements are critical to the 2018 Palu, Sulawesi tsunami. *Pure Appl. Geophys.* 176(10):4069–109

Vannucchi P, Spagnuolo E, Aretusini S, Di Toro G, Ujiie K, et al. 2017. Past seismic slip-to-the-trench recorded in Central America megathrust. *Nat. Geosci.* 10(12):935–40

Vermilye JM, Scholz CH. 1998. The process zone: a microstructural view of fault growth. *J. Geophys. Res.* 103(B6):12223–37

Viesca RC, Garagash DI. 2015. Ubiquitous weakening of faults due to thermal pressurization. *Nat. Geosci.* 8(11):875–79

Violay M, Nielsen S, Gibert B, Spagnuolo E, Cavallo A, et al. 2014. Effect of water on the frictional behavior of cohesive rocks during earthquakes. *Geology* 42(1):27–30

Violay M, Nielsen S, Spagnuolo E, Cinti D, Di Toro G, Di Stefano G. 2013. Pore fluid in experimental calcite-bearing faults: abrupt weakening and geochemical signature of co-seismic processes. *Earth Planet. Sci. Lett.* 361:74–84

Wawersik WR, Brace WF. 1971. Post-failure behavior of a granite and diabase. *Rock Mech.* 3(2):61–85

Wibberley CAJ, Shimamoto T. 2003. Internal structure and permeability of major strike-slip fault zones: the Median Tectonic Line in Mie Prefecture, Southwest Japan. *J. Struct. Geol.* 25(1):59–78

Wibberley CAJ, Shimamoto T. 2005. Earthquake slip weakening and asperities explained by thermal pressurization. *Nature* 436(7051):689–92

Wibberley CAJ, Yielding G, Di Toro G. 2008. Recent advances in the understanding of fault zone internal structure: a review. *Geol. Soc. Lond. Spec. Publ.* 299(1):5–33

Wilson B, Dewers T, Reches Z, Brune J. 2005. Particle size and energetics of gouge from earthquake rupture zones. *Nature* 434(7034):749–52

Wong T-F. 1982. Shear fracture energy of Westerly granite from post-failure behavior. *J. Geophys. Res.* 87(B2):990–1000

Wong T-F. 1986. On the normal stress dependence of the shear fracture energy. In *Earthquake Source Mechanics*, ed. S Das, J Boatwright, CH Scholz, pp. 1–11. Washington, DC: AGU

Yao L, Ma S, Shimamoto T, Togo T. 2013. Structures and high-velocity frictional properties of the Pingxi fault zone in the Longmenshan fault system, Sichuan, China, activated during the 2008 Wenchuan earthquake. *Tectonophysics* 599:135–56

Yoshimitsu N, Kawakata H, Takahashi N. 2014. Magnitude −7 level earthquakes: a new lower limit of self-similarity in seismic scaling relationships. *Geophys. Res. Lett.* 41(13):4495–502

Annual Review
of Earth and
Planetary Sciences
Volume 51, 2023

Contents

Errata

An online log of corrections to *Annual Review of Earth and Planetary Sciences* articles may be found at http://www.annualreviews.org/errata/earth

Related Articles

From the ***Annual Review of Astronomy and Astrophysics***, Volume 60 (2022)

Atmospheres of Rocky Exoplanets
Robin Wordsworth and Laura Kreidberg

From the ***Annual Review of Chemical and Biomolecular Engineering***, Volume 13 (2022)

Direct Air Capture of CO_2 Using Solvents
Radu Custelcean

Technological Options for Direct Air Capture: A Comparative Process Engineering Review
Xiaowei Wu, Ramanan Krishnamoorti, and Praveen Bollini

From the ***Annual Review of Ecology, Evolution, and Systematics***, Volume 53 (2022)

Evolutionary Ecology of Fire
Jon E. Keeley and Juli G. Pausas

Integrating Fossil Observations Into Phylogenetics Using the Fossilized Birth–Death Model
April M. Wright, David W. Bapst, Joëlle Barido-Sottani, and Rachel C.M. Warnock

The Macroevolutionary History of Bony Fishes: A Paleontological View
Matt Friedman

From the ***Annual Review of Environment and Resources***, Volume 47 (2022)

The Ocean Carbon Cycle
Tim DeVries

Permafrost and Climate Change: Carbon Cycle Feedbacks From the Warming Arctic
Edward A.G. Schuur, Benjamin W. Abbott, Roisin Commane, Jessica Ernakovich, Eugenie Euskirchen, Gustaf Hugelius, Guido Grosse, Miriam Jones, Charlie Koven, Victor Leshyk, David Lawrence, Michael M. Loranty, Marguerite Mauritz, David Olefeldt, Susan Natali, Heidi Rodenhizer, Verity Salmon, Christina Schädel, Jens Strauss, Claire Treat, and Merritt Turetsky

Remote Sensing the Ocean Biosphere
Sam Purkis and Ved Chirayath

From the ***Annual Review of Fluid Mechanics***, Volume 55 (2023)

Submesoscale Dynamics in the Upper Ocean
John R. Taylor and Andrew F. Thompson

Fluid Dynamics of Polar Vortices on Earth, Mars, and Titan
Darryn W. Waugh

Icebergs Melting
Claudia Cenedese and Fiamma Straneo

The Fluid Mechanics of Deep-Sea Mining
Thomas Peacock and Raphael Ouillon

Turbulent Rotating Rayleigh–Bénard Convection
Robert E. Ecke and Olga Shishkina

From the ***Annual Review of Marine Science***, Volume 15 (2023)

From Stamps to Parabolas
S. George Philander

Sociotechnical Considerations About Ocean Carbon Dioxide Removal
Sarah R. Cooley, Sonja Klinsky, David R. Morrow, and Terre Satterfield

Nuclear Reprocessing Tracers Illuminate Flow Features and Connectivity Between the Arctic and Subpolar North Atlantic Oceans
Núria Casacuberta and John N. Smith

The Arctic Ocean's Beaufort Gyre
Mary-Louise Timmermans and John M. Toole

Global Quaternary Carbonate Burial: Proxy- and Model-Based Reconstructions and Persisting Uncertainties
Madison Wood, Christopher T. Hayes, and Adina Paytan

Quantifying the Ocean's Biological Pump and Its Carbon Cycle Impacts on Global Scales
David A. Siegel, Timothy DeVries, Ivona Cetinić, and Kelsey M. Bisson

Novel Insights into Marine Iron Biogeochemistry from Iron Isotopes
Jessica N. Fitzsimmons and Tim M. Conway

Insights from Fossil-Bound Nitrogen Isotopes in Diatoms, Foraminifera, and Corals
Rebecca S. Robinson, Sandi M. Smart, Jonathan D. Cybulski, Kelton W. McMahon, Basia Marcks, and Catherine Nowakowski

Prokaryotic Life in the Deep Ocean's Water Column
Gerhard J. Herndl, Barbara Bayer, Federico Baltar, and Thomas Reinthaler

Lipid Biogeochemistry and Modern Lipidomic Techniques
Bethanie R. Edwards

From the ***Annual Review of Materials Research***, Volume 52 (2022)

Biomineralized Materials for Sustainable and Durable Construction
Danielle N. Beatty, Sarah L. Williams, and Wil V. Srubar III

Brittle Solids: From Physics and Chemistry to Materials Applications
Brian R. Lawn and David B. Marshall

Material Flows and Efficiency
Jonathan M. Cullen and Daniel R. Cooper

Architectural Glass
Sheldon M. Wiederhorn and David R. Clarke